Neogene South Asian monsoon rainfall and wind histories diverged due to topographic effects

Anta-Clarisse Sarr, Yannick Donnadieu, C. T. Bolton, Jean-Baptiste Ladant, Alexis Licht, Frédéric Fluteau, Marie Laugié, Delphine Tardif, Guillaume Dupont-Nivet

Neogene South Asian Monsoon Rainfall and Wind Histories diverged due to topography effects

Anta-Clarisse Sarr[1,*], Yannick Donnadieu[1], Clara T. Bolton[1], Jean-Baptiste Ladant[2], Alexis Licht[1], Frédéric Fluteau[3], Marie Laugié[1], Delphine Tardif[1,3], Guillaume Dupont-Nivet[4,5]

[1] Aix Marseille Univ, CNRS, IRD, INRAE, Coll. France, CEREGE, Aix-en-Provence, France.

[2] Laboratoire des Sciences du Climat et de l'Environnement, LSCE/IPSL, CEA-CNRS-UVSQ, Université Paris-Saclay, 91191 Gif-sur-Yvette, France.

[3] Institut de physique du globe de Paris, CNRS, Université de Paris, 75005 Paris, France.

[4] Géosciences Rennes, UMR CNRS 6118, Université de Rennes, 35000 Rennes, France.

[5] Institute of Geosciences, Potsdam University, Potsdam, Germany.

* Correspondence and requests for materials should be addressed to Anta-Clarisse Sarr (sarr@cerege.fr)

The drivers of South Asian Monsoon evolution remain highly debated. An intensification of monsoonal rainfall recorded in terrestrial and marine sediment archives from the earliest Miocene (23-20 million years ago, Ma) is generally attributed to Himalayan uplift. However, Indian Ocean paleorecords place the onset of a strong monsoon around 13 Ma, linked to strengthening of the southwesterly winds of the Somali Jet that also force Arabian Sea upwelling. Here we reconcile these divergent records using Earth System Model simulations to evaluate the interactions between paleogeography and ocean-atmosphere dynamics. We show that factors forcing South Asian Monsoon circulation versus rainfall are decoupled and diachronous. Himalayan and Tibetan Plateau topography predominantly controlled early Miocene rainfall patterns, with limited impact on ocean-

atmosphere circulation. Yet the uplift of East African and Middle Eastern topography played a pivotal role in the establishment of modern Somali Jet structure above the western Indian Ocean, while strong upwelling initiates as a direct consequence of the Arabian Peninsula emergence and the initiation of modern-like atmospheric circulation. Our results emphasize that although elevated rainfall seasonality was likely a persistent feature since the India-Asia collision in the Paleogene, the modern-like monsoonal atmospheric circulation was only reached in the late Neogene.

The South Asian monsoon (SAM) is a key element of Asian climate that sustains populations over a vast region *via* continental rainfall and wind-driven coastal upwelling supporting important marine ecosystem services. Assessing past SAM evolution and underlying mechanisms is therefore essential to understand its behavior in warm climate conditions and to better constrain feedbacks with topography and global climate on geological timescales[1]. A sound understanding of factors controlling past monsoonal changes is, however, hampered by apparently conflicting interpretations of monsoon proxies[2-10]. Isotopic and botanical records indicate the existence of strong seasonal SAM rainfall on land since at least the Paleogene[3,4], while sedimentary archives of monsoon-driven erosion and weathering in the Himalayan foreland and northern Indian Ocean suggest an important intensification of monsoonal rainfall around 25-20 million years ago (Ma), peaking at 15 Ma[5]. In contrast, a late middle Miocene (~13 Ma) onset of the 'modern-like' SAM has been inferred from ocean sediment archives in the western Arabian Sea (ODP sites 722 and 730)[6-10] and Maldives archipelago (IODP expedition

359)[11] (Fig. 1a). Those records indicate the onset of strong wind-driven coastal upwelling in the western Arabian Sea, associated with high primary production and oxygen minimum zone, and a reorganization of tropical Indian Ocean surface circulation attributed to the inception of low-level winds with a strength and/or pattern similar to today (Fig. 1a). The mechanism(s) driving this relatively late appearance of 'modern-like' monsoon circulation[6,7,11], well after Himalayan uplift[12,13] that is nonetheless generally accepted as the main driver of SAM intensification[5,6,13-14], remains uncertain.

The apparent decoupling between monsoon rainfall and winds during the early to middle Miocene (23-11 Ma) either suggests that regional proxy records are not all faithfully recording monsoon strength or that we need to reassess the widely-held view that Himalaya-Tibetan Plateau elevation is the primary control on both SAM wind and rainfall intensity[17,18]. Previous modeling studies highlighted the sensitivity of the SAM to regional topography[17,19-22] and advanced our mechanistic understanding of SAM forcing and the complex relationship between atmospheric circulation, rainfall, and orography[17]. Yet the degree of coupling between these parameters in the past remains poorly understood because, to date, such studies have not considered land-sea distribution despite its important role in controlling monsoon dynamics[23-24]. Additionally, past atmospheric dynamics, surface ocean circulation and marine biogeochemistry need to be assessed together to enable realistic comparisons with marine records used to trace past monsoon circulation.

Here we investigate both SAM evolution and biological productivity in the western Arabian sea during the Miocene with an Earth System Model (IPSL-CM5A2[25]), combined with an offline ocean biogeochemistry component (PISCES-v2[26]) (see Methods). We performed the experiments using realistic land-sea configurations at ~20 Ma (early Miocene, hereafter EM) and ~10 Ma (late Miocene, hereafter LM) (See Methods, Fig. 1 and Extended Data Figure 1). This allows us to assess the relationship between the Somali Jet, the dominant low-level wind pattern above the Arabian Sea (Fig. 1a), and western Arabian Sea upwelling during the Miocene. We then investigate the potential influence of Miocene paleogeographic and global climate changes on Somali Jet structure and SAM rainfall intensity using sensitivity experiments. Our results reveal that drivers of ocean-atmosphere dynamical changes in the western Arabian sea are decoupled from drivers of rainfall patterns in continental Asia since the Miocene.

Miocene upwelling and primary productivity

Our simulations show that primary productivity in the western Arabian Sea increases (Fig. 2a) and becomes strongly seasonal (Fig. 2b) in response to paleogeographic changes from the early to late Miocene. In the EM simulation, primary productivity in the surface ocean (0-40 meters depth) is limited by low nutrient availability (Fig. 2b), restricting biological production to the deep photic zone (60-120m) where sufficient nutrients and light are available (Fig. 2c). In contrast, primary productivity in the LM simulation is highly seasonal, with maximum values during late boreal summer (August-September) (Fig. 2b) sustained by increased nutrient delivery to the euphotic zone relative to EM (Fig. 2b-c).

The seasonal availability of nutrients therefore imposes a substantial constraint on summer productivity in this region and its enhancement in LM relative to EM allows productivity to increase. In the present-day western Arabian Sea, the nutrient enrichment in the surface layer that fuels the seasonal increase in productivity during summer is induced by vertical advection due to upwelling generated by Ekman transport and to wind-driven convective mixing forced by the south-westerly monsoon winds[26]. The LM simulation depicts atmosphere-ocean interactions in the Arabian Sea that resemble the modern, characterized by strong early summer (JJA) upwelling alongshore Oman and Somalia (locally reaching 1.5 $m.day^{-1}$ upward velocity) and a deepening of the mixed layer (up to 100 m) in the western area (Fig. 2b and 3a and Extended Data Figure 2d). These processes are driven by the south-westerly Somali Jet that generate wind stress off the coasts of Somalia and the Arabian Peninsula (Fig. 3d and 3g). The lack of upwelling in the EM simulation is due to a different Somali Jet strength and pattern with weaker surface and low-level (850 hPa) winds (-6 to -8 $m.s^{-1}$ in the core of the jet compared to LM) broadly shifted equatorward and a more zonal flow between 0°N-20°N (Fig 3d-e). Consequently, the wind-stress alongshore the Arabian Peninsula decreases (Fig. 3g-i), leading to weaker upwelling (less than 0.6 $m.day^{-1}$ upward velocity) and a flat and shallow (20 m) mixed layer in the whole region (Fig. 3b and Extended Data Figure 2) that prevents nutrient entrainment into surface waters inhibiting productivity. SSTs in the western Arabian Sea are on average 4°C warmer in the EM simulation (Extended Data Figure 2a), because the area receives warm waters from the Neotethyan embayment rather than cooler waters from the equatorial upwelling region advected northwards by the eastern

119 African coastal currents. EM and LM simulations indicate that the onset of seasonally high
120 productivity in the western Arabian Sea as well as SST cooling is caused by a modification
121 of surface ocean circulation, driven by the inception of a Somali Jet similar in structure
122 and intensity to its modern counterpart.

123

124 **Drivers of modern-like SAM winds and rainfall patterns**

125 Further experiments were conducted to assess the mechanisms responsible for the
126 evolution of the Somali Jet and upwelling system during the Miocene. These additional
127 simulations allow us to disentangle the effects of regional paleogeographic evolution and
128 contemporaneous global changes (expanded Antarctic ice-sheet and lower atmospheric
129 CO_2 concentration) on ocean-atmosphere dynamics (Fig. 1, Extended Data Table 1 and
130 Figure 3 and Methods). Major Miocene paleogeographic changes that we considered are
131 the rise of the complex orogen extending from the Anatolian to the Iranian Plateau, the
132 uplift of the East African Highlands and the Himalaya-Tibetan Plateau complex, and the
133 emergence of land in Eastern Arabian Peninsula. Results are synthesized in Figure 4a-
134 b.

135 The most salient outcome of these sensitivity experiments is the key role played by the
136 Middle East physiography in the onset of modern-like atmosphere-ocean dynamics in the
137 Arabian Sea. Removing the Anatolia-Iran orogen (LM-NoAIO vs. LM) significantly
138 reduces wind strength north of 10°N (Extended Data Figure 4c) and weakens upwelling
139 alongshore Oman (Fig. 4a). Additionally submerging the Eastern Arabian Peninsula (LM-

NoEAP) in the LM configuration results in the disappearance of the upwelling zone (Fig. 3c and 4a). In LM-NoEAP, the Arabian Peninsula immersion suppresses the westward extension of the HTP low pressure anomaly (Extended Data Figure 5). As a result, the model simulates a decrease in south-westerly winds blowing above the western Arabian Sea towards the Indian subcontinent (Fig. 3d,f) and a limited northward expansion of the Somali Jet (Fig 3d,f). Both effects contribute to decreasing the wind stress along the Oman coastlines (Fig. 3g,i), which, in turn, modifies the surface circulation in the western Arabian Sea suppressing upwelling. Meanwhile, expanding the Antarctic ice-sheet (LM-AIS) and reducing atmospheric pCO_2 levels (LM-CO_2) only marginally affect Somali Jet intensity or upwelling (Fig. 4a-b and Extended Data Figure 4a-b), although the imposed pCO_2 decrease results in surface cooling of 1.5°C in the western Arabian Sea (LM-CO_2 vs. LM). Cumulated with the ~4°C regional SST cooling induced by the early to late Miocene paleogeographic evolution, our simulations yield a total SST decrease in agreement with proxy reconstructions (~7°C) at nearby drill sites (ODP 722 and 730)[10]. Conversely, sensitivity experiments for the early Miocene with modern HTP (EM-HTP), or higher than present-day Himalayan elevation (EM-Him)[4] show only a marginal impact on atmosphere-ocean interactions in the Arabian Sea (Fig. 4a-b). Sufficiently high East African Highlands help precondition the modern Somali Jet pattern by forcing the cross-equatorial flow to bend (Fig. 4b and Extended Data Figure 4d)[19-20]. However, changes mainly affect upwelling alongshore Somalia (EM-EAH vs. EM) (Fig 4a) because of restructuring of the jet located in the equatorial area (0-10°N).

In addition to its imprint on Arabian Sea surface oceanography, we assess, for each simulation, the intensity of monsoonal circulation through the Webster-Yang Index[30], which traces the vigor of atmospheric circulation (Fig. 4c). The intensity of large-scale circulation is preserved in LM simulations regardless of Anatolia-Iran topography or land extent on the Arabian Peninsula. In contrast, all of our EM simulations are characterized by a weaker circulation (Fig. 4c), likely due to the remote control of the large Paratethys Sea on pressure systems[24,31].

Our results thus corroborate the hypothesis that the western Arabian Sea upwelling system and associated high primary productivity initiated in response to the full development of the "modern-like" Somali jet[6,11], which we show was a direct result of the emergence of the Eastern Arabian Peninsula, preconditioned by the East African Highlands and amplified by Anatolia-Iran topography. As the Arabian Peninsula paleogeographic evolution during the Miocene responded both to the long-term Arabia-Eurasia collision[32] and to eustatic variations, we hypothesize an indirect contribution of the Antarctica ice-sheet whereby the Mi-3 (13.8 Ma, ~ 50 m) and Mi-4 (12.9 Ma, ~ 20-30 m) sea-level retreats[33] increased the emerged surface area of the Eastern Arabian Peninsula and forced abrupt changes[11] in regional atmosphere-ocean dynamics. Importantly, our simulations show that the Miocene intensifications of wind strength and upwelling inferred from western Indian Ocean palaeoceanographic records are not directly tied to the evolution of the HTP complex as has often been assumed[6,7,10,15,16].

Continental rainfall changes are temporally decoupled from Arabian Sea upwelling changes. Although the full emergence of the Arabian Peninsula in the LM is instrumental

183 in driving the onset of Oman upwelling, it does not markedly alter either of the precipitation
184 metrics (Fig 4a,d-e and Extended Data Figure 6 and 7) because moisture transport by
185 the Somali Jet to peninsular India only slightly increases (Extended Data Figure 8f). In
186 contrast, the Anatolia-Iran uplift enhances both upwelling and summer precipitation on
187 Himalayan topography and South Asian lowlands (Fig 4d-e and Extended Data Figure 6
188 and 7). Anatolia-Iran Plateau uplift deepens the low-pressure area over the Arabian
189 Peninsula, enhancing low-level wind intensity and moisture transport from the Arabian
190 Sea toward the South-Asian landmass (Extended Data Figure 8e). EM, increasing
191 topography in the HTP region alone (EM-HTP and EM-Him) increases summer
192 precipitation and seasonality over the region's highlands (Fig. 4d and Extended Data
193 Figure 6-7), while the Somali Jet and upwelling intensity are only marginally affected (Fig
194 4a-b). These results corroborate the hypothesis that the increases seen in sedimentary
195 and weathering fluxes between 25 and 15 Ma could be partly associated with monsoon
196 intensification related to coeval uplift of the Himalayan ranges[5], although weathering rates
197 would also be sensitive to change in exhumation rates recorded at that time.
198
199 **Reconciling divergent South Asian Monsoon records**

200 The history of the SAM remains hotly debated as new paleoceanographic and continental
201 records emerge and propose contradictory timing for the onset of modern-like Asian
202 monsoons[3,6,11,31,34-37]. Our new set of climate simulations shows that these apparent
203 contradictions can be reconciled. From our results we infer that seasonally intense
204 precipitation in South Asia existed in the early Miocene and probably earlier, as suggested

by continental records and paleoclimate models[3,31,37], but that a modern-like structure and vigor of the SAM atmospheric circulation developed in the late middle Miocene as a result of regional changes in Middle-East and East-Africa, in agreement with multi-proxy palaeoceanographic records[6,7,10,11]. This polygenetic history of the SAM is coherent with the proposed Neogene transition from an 'ITCZ-dominated' to a 'land-sea breeze-dominated' monsoon[4,37] based on botanical evidence. Here, we show that this transition towards the modern monsoon system is independent of Asian orography but is forced by geographical evolution at the western boundary of the Indian Ocean.

This emerging view does not preclude an important role for the Himalaya-Tibet orogeny in strengthening rainfall amount and in the establishment of a longer rainy season (similar to modern) in the early Miocene or before[5,13,38]. However, our results do indicate that HTP tectonic activity cannot be held to account for either the palaeoceanographic changes observed in the Arabian Sea and equatorial Indian Ocean, or for the establishment of modern-like large-scale atmospheric circulation with a strong Somali Jet. Our results further emphasize the important role of the Iran-Zagros orogen on monsoonal rainfall in agreement with ref.17. Hence, while much of the effort to understand the evolution of Cenozoic Asian monsoons has focused on the Himalaya-Tibet region, we underscore that constraining the exact timing of East African and Middle Eastern physiographic changes is crucial to grasp the full complexity of Asian monsoon evolution. Determining the timing of the initiation of a "true" modern SAM is a semantic issue, the answer to which depends on which metric primarily defines the modern SAM: the atmospheric circulation and regional atmosphere-ocean dynamics, the rainfall intensity, or the seasonal

distribution of rainfall. We have shown here that, on geological timescales, these three parameters are not controlled by the same factors and likely had independent histories.

Acknowledgments: We thank the CEA/CCRT for providing access to the HPC resources of TGCC under the allocation 2018-A0030102212, 2019-A0050102212 and 2020-A0090102212 made by GENCI and French ANR project AMOR (ANR-16-CE31-0020) (YD) for providing funding for this work. Colored figures in this paper were made with perceptually uniform, color-vision-deficiency-friendly scientific color maps, developed and distributed by Fabio Crameri (https://www.fabiocrameri.ch/colourmaps/). We thank Christian Ethé, Laurent Bopp and Olivier Aumont for technical help in adapting PISCES to deep-time configurations.

Author contributions: A-CS and YD designed the study and ran the simulations. FF provides updated paleogeographies and expertise on paleogeography evolution. JBL and ML developed and ran the tests for the run-off adapted version of PISCES and help with the setup of PISCES simulations. CTB helped compile and synthesize paleoceanographic records. A-CS, YD, CTB, AL and JBL wrote the manuscript. GDN, FF and DT provided substantial comments and revisions.

Competing interests: Authors declare no competing interests.

Figure captions:

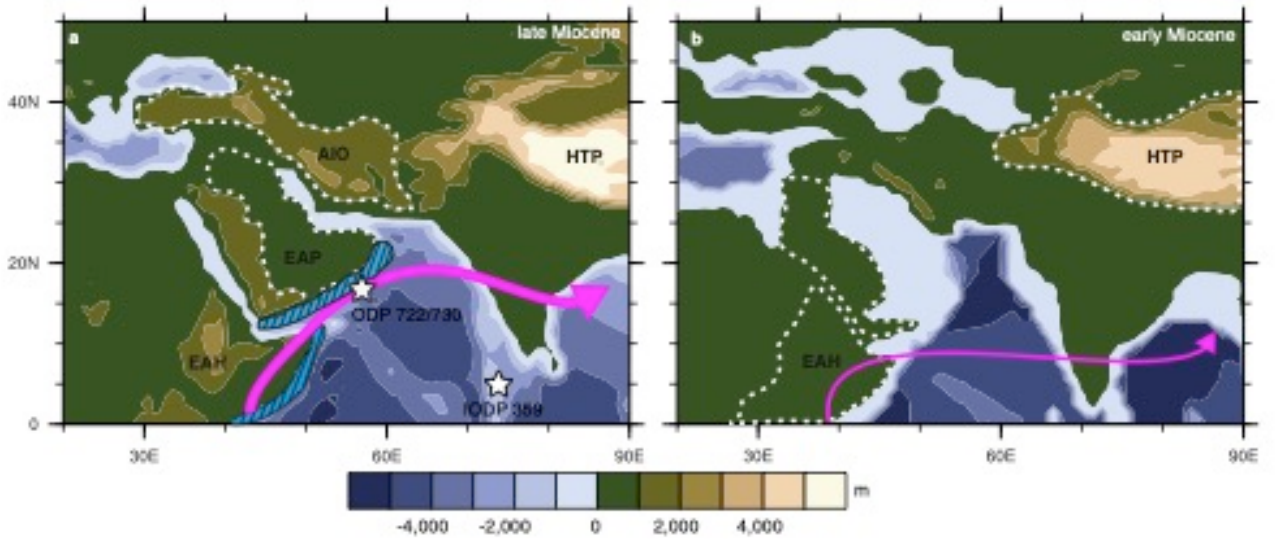

Fig. 1. Western Indian Ocean paleogeographic reconstructions. (a) late Miocene (~10 Ma) (this study, updated from ref. 27, see Methods) ; (b) early Miocene (~20 Ma)[28]. EAH - East African Highlands; AIO – Anatolian-Iran Orogen; HTP - Himalaya-Tibetan Plateau; EAP - East Arabian Peninsula. Present-day geography and ocean-atmosphere dynamics resemble the late Miocene in this region. Dashed contours show areas where modifications are applied in sensitivity experiments (see Methods and Extended Data Table 1 and Figure 3 for detailed descriptions). Simulated Somali Jet patterns and strengths are represented by the magenta arrows. Blue stretched areas show upwelling location from simulations. Stars show the location of drilling sites or expeditions cited in the text. IODP - International Ocean Discovery Program; ODP - Ocean Drilling Program.

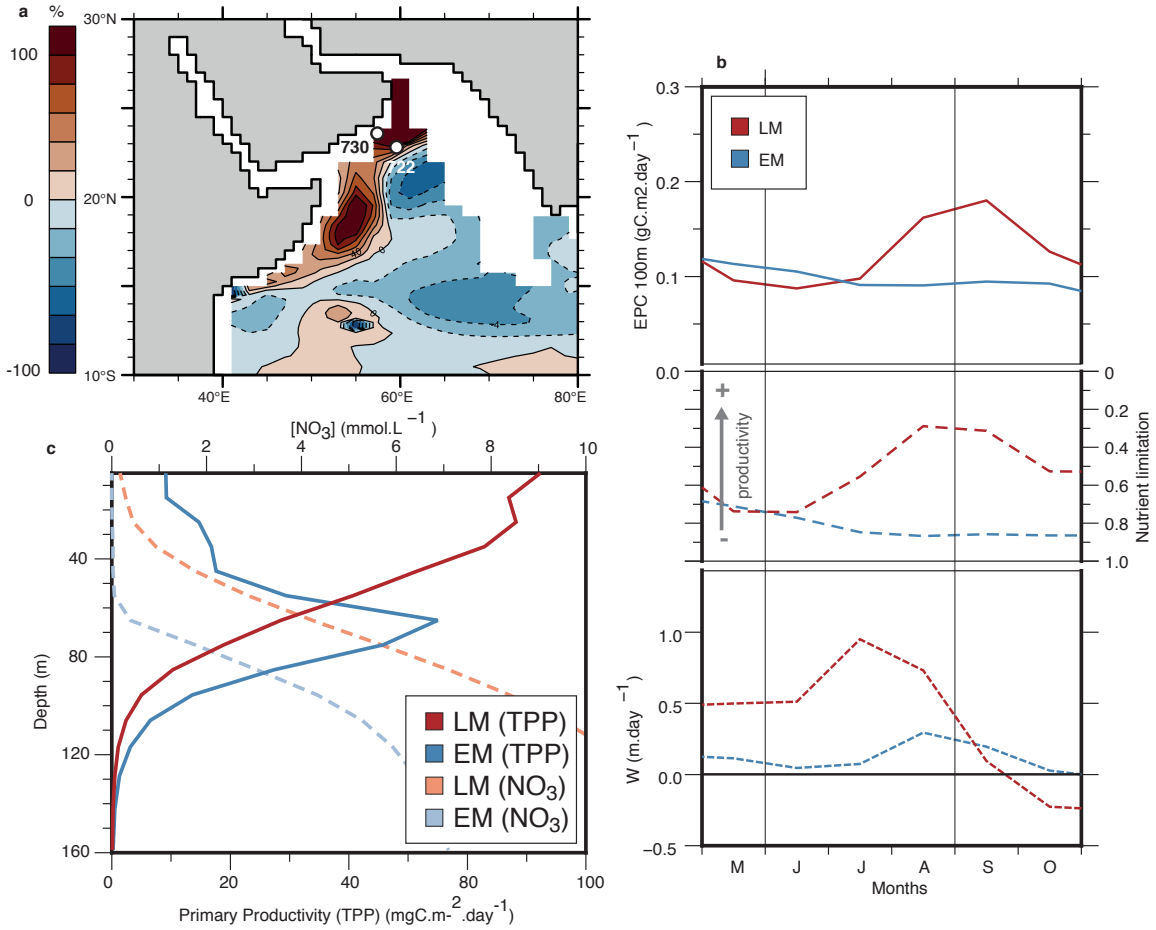

Fig. 2. Change in Arabian Sea productivity between the early and late Miocene. (a) Change in Export Production at 100m (EPC 100m) between early Miocene (EM) and late Miocene (LM) simulations during late summer (August-October). ODP Sites 722 and 730 are shown on the map; (b) Seasonal variation of EPC 100m along the Oman Margin ($gC.m^{-2}.day^{-1}$) (averaged along coastal grid points north of 15°N), nutrient limitation (averaged over 0-60 m, note inverted axis), and mean vertical velocity (W) at 80 m ($m.day^{-1}$). A limitation term of zero indicates no nutrient limitation. In panels a and b, Export Production at 100 m (EPC 100m), a commonly used measure of the carbon export to the deep ocean that is ultimately recorded in sediments, is shown instead of Primary Productivity but the two exhibit similar temporal behavior; (c) July-October cumulated

Total Primary Productivity (TPP, $mgC.m^{-2}.day^{-1}$, solid lines) and averaged Nitrate concentration (NO_3, $mmol.L^{-1}$, dashed lines) with depth for EM and LM.

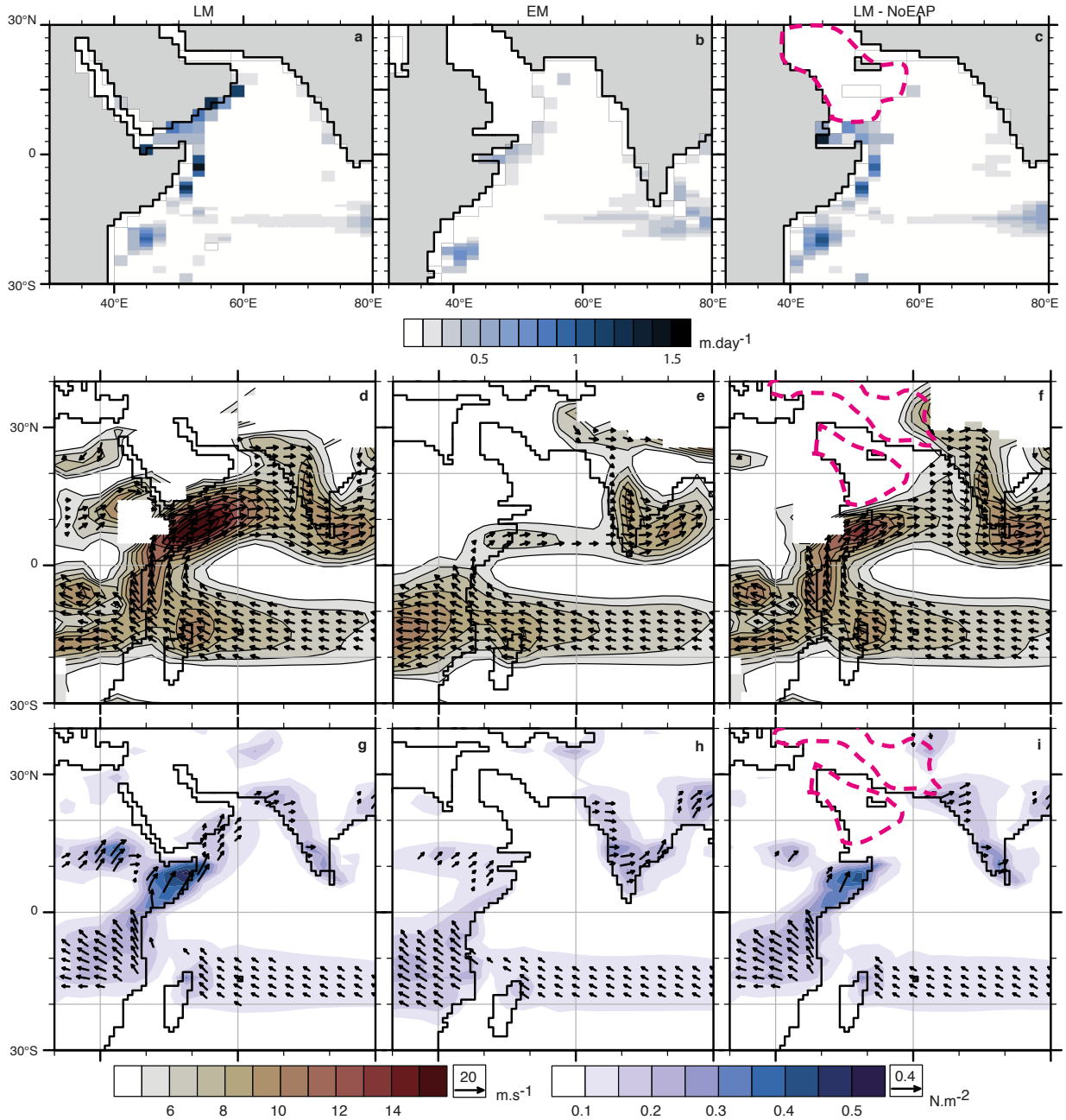

Fig. 3. Changes in ocean-atmosphere dynamics in response to Miocene paleogeographic evolution. Top: Upwelling velocity (vertical velocity at 80 m depth, averaged over JJA); Middle: Low level winds (850 hPa) during boreal summer (JJA);

Bottom: Wind stress during boreal summer (JJA).(a), (d) and (g) - late Miocene (LM) and (b), (e) and (h) – early Miocene (EM) simulations; (c), (f) and (i) LM-NoEAP. LM-NoEAP is a simulation without the Eastern Arabian Peninsula (EAP), designed to show the influence of Arabian Peninsula immersion on the Somali Jet structure in a LM configuration. Dashed pink contours on panels (c), (f) and (i) indicate the location of geographic modifications compared to LM simulation (panels (a), (d) and (g)).

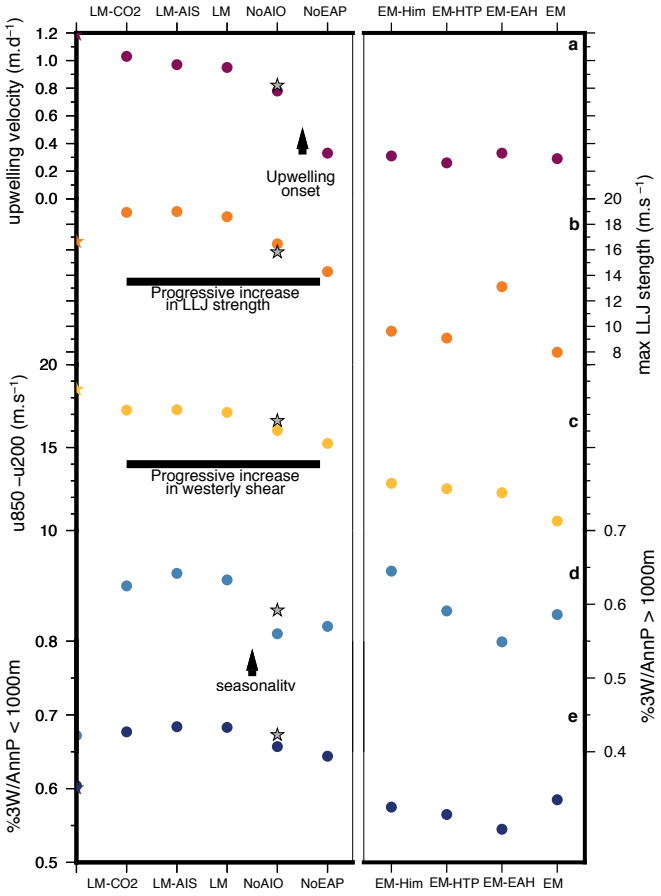

Fig. 4. South Asian Monsoon circulation and rainfall in sensitivity experiments. (a) Maximum summer (JJA) vertical velocity at 80 m averaged over coastal grid points north of 15°N ; (b) maximum intensity of the Somali Jet over the Arabian Sea (averaged over JJA, [30-60°E, 0-20°N]); (c) Webster-Yang Index (Meridional wind stress shear

(u850hPa-u200hPa) averaged over [40-110°E, 0-20°N] and June-September)[30] ; (d) 3 consecutive wettest months relative to annual mean precipitation [65-95°E, 0-35°N, see Extended Data Figure 6] for high-elevation areas (over 1,000 m - light blue) and e) for Indian foreland (below 1,000 m - dark blue). A 1,000 m threshold was chosen to distinguish low-land areas of the Indian subcontinent from high topography of the Himalaya-Tibetan Plateau (HTP) at the model grid resolution. Seasonality changes are mostly driven by changes in summer rainfall amount (Extended Data Figure 6 and 7). Colored stars indicate values for a pre-industrial simulation[25]. Gray star indicates LM-NoEAHR simulation which account for uncertainties in late Miocene East African Highland (EAH) elevation (see "Methods"). Simulation characteristics can be found in Extended Data Table 1 and Extended Data Figure 1 and 3.

References

1. Raymo, M. E. & Ruddiman, W. F. Tectonic forcing of late Cenozoic climate. *Nature* **359**, 117-122 (1992).
2. Kroon, D., Steens, T.N.F & Troelstra, S. R. Onset of Monsoon Related Upwelling in the Western Arabian Sea as revealed by Planktonic Foraminifers. *Proc. Oce. Drill. Prog., scientific results* **11** (1991).
3. Licht, A. *et al.* Asian monsoons in a late Eocene greenhouse world. *Nature* **513**, 501–506 (2014).

4. Bhatia, H. *et al.*, Late Cretaceous–Paleogene Indian monsoon climate vis-à-vis movement of the Indian plate, and the birth of the South Asian Monsoon, *Gondwana Research* **93**, 89-100 (2021).
5. Clift, P. D. & Webb, A. A. G. history of the Asian monsoon and its interactions with solid earth tectonics in Cenozoic South Asia*. Geological Society, London, Special Publications* **483**, , 875–880 (2019).
6. Gupta, A.K., Yuvaraja, A., Prakasam, M., Clemens, S.C. & Velu, A. Evolution of the South Asian monsoon wind system since the late Middle Miocene. *Palaeogeogr. Palaeoclimatol. Palaeoecol.* **438**, 160–167 (2015).
7. Bialik, O. M. *et al.*, Monsoons, Upwelling, and the Deoxygenation of the Northwestern Indian Ocean in Response to Middle to Late Miocene Global Climatic Shifts*. Paleoceanogr. Paleoclimatology* **35**, e2019PA003762 (2020).
8. Nigrini, C. Composition and biostratigraphy of radiolarian assemblages from an area of upwelling (northwestern arabian sea, lag 117). *Proc. Oce. Drill. Prog.,* s*cientific results* **117**, 89–126 (1991).
9. Huang, Y., Clemens, S. C., Liu, W., Wang, Y., & Prell, W. L. Large-scale hydrological change drove the late Miocene C4 plant expansion in the Himalayan foreland and Arabian peninsula*. Geology* **35**, 531–534 (2007).
10. Zhuang, G., Pagani, M., Zhang, Y. G. Monsoonal upwelling in the western Arabian Sea since the middle Miocene*. Geology* **45**, 655–658 (2017).
11. Betzler, C. *et al.*, The abrupt onset of the modern South Asian Monsoon winds. *Sci. Reports* **6**, 1–10 (2016).

12. Gébelin, A. *et al.*, The Miocene elevation of mount Everest. *Geology* **41**, 799-802 (2013).
13. Ding, L. *et al.*, Quantifying the rise of the Himalaya orogen and implications for the South Asian Monsoon. *Geology* **45**, 215–218 (2017).
14. Prell, W. L. & Kutzbach, J. E. Sensitivity of the Indian monsoon to forcing parameters and implications for its evolution. *Nature* **360**, 647–652 (1992).
15. Tada, R., Zheng, H. & Clift, P. D. Evolution and variability of the Asian monsoon and its potential linkage with uplift of the Himalaya and Tibetan plateau. *Prog. Earth Planet. Sci.* **3**, 4 (2016).
16. Molnar, P., Boos, W. R. & Battisti, D. S. Orographic Controls on Climate and Paleoclimate of Asia: Thermal and Mechanical Roles for the Tibetan Plateau . *Annu. Rev. Earth Planet. Sci.* **38**, 77–102 (2010).
17. Acosta, R. P. & Huber, M. Competing topographic mechanisms for the Summer Indo-Asian Monsoon. *Geophysi. Res. Lett. **47,*** e2019GL085112 (2020).
18. Thomson, J. R. *et al*. Tectonic and climatic drivers of Asian monsoon evolution. *Nat. Commun. **12,*** 4022 (2021).
19. Chakraborty, A., Nanjundiah, R. S. & Srinivasan, J. Impact of African orography and the Indian summer monsoon on the low-level Somali jet . *Int. J. Clim.* **29**, 983–992 (2009).
20. Wei, H.-H. & Bordoni, S. On the Role of the African Topography in the South Asian Monsoon. *J. Atm. Sci.* **73**, 3197–3212 (2016).

21. Tang, H., Micheels, A., Eronen, J. T., Ahrens, B. & Fortelius, M. Asynchronous responses of East Asian and Indian summer monsoons to mountain uplift shown by regional climate modelling experiments. *Clim. Dyn.* **40**, 1531–1549 (2013).
22. Zhang, R., Jiang, D., Zhang, Z. & Yu, E. The impact of regional uplift of the Tibetan Plateau on the Asian monsoon climate . *Palaeogeogr. Palaeoclimatol., Palaeoecol.* **417**, 137–150 (2015).
23. Zhang, Z. *et al.* Aridification of the Sahara desert caused by Tethys Sea shrinkage during the Late Miocene. *Nature* **513**, 401–404 (2014).
24. Fluteau, F., Ramstein, G. & Besse, J. Simulating the evolution of the Asian and African monsoons during the past 30 Myr using an atmospheric general circulation model. *J. Geophys. Res. Atmospheres* **104**, 11995–12018 (1999).
25. Sepulchre, P. *et al.* IPSL-CM5A2–An Earth System Model designed for multi-millennial climate simulations. *Geosci. Model Dev.* **13**, 3011–3053 (2020).
26. Aumont, O., Ethé, C., Tagliabue, A., Bopp, L. & Gehlen, M. PISCES-v2: an ocean biogeochemical model for carbon and ecosystem studies. *Geosci. Model Dev.* **8**, 2465–2513 (2015).
27. Dowsett, H. *et al*. The PRISM4 (mid-Piacenzian) paleoenvironmental reconstruction. *Clim. Past* **12**, 1519–1538 (2016).
28. Poblete, F. *et al.,* Towards interactive global paleogeographic maps, new reconstructions at 60, 40 and 20 Ma. Earth-Science Rev 214, 103508 (2021)
29. Koné, V., Aumont, O., Lévy, M. & Resplandy, L. Physical and biogeochemical controls of the phytoplankton seasonal cycle in the Indian ocean: A modeling

study. *Indian Ocean Biogeochemical Processes and Ecological Variability* **185**, 147-166 (2009).

30. Webster, P. J. & Yang, S. Monsoon and ENSO: Selectively interactive systems. *Quarterly Journal of the Royal Meteorological Society* **118**, 877-926 (1992).
31. Tardif, D. *et al.* The origin of Asian monsoons: a modelling perspective. *Clim. Past* **16**, 847–865 (2020).
32. McQuarrie, N., & van Hinsbergen, D. J. Retrodeforming the Arabia-Eurasia collision zone: Age of collision versus magnitude of continental subduction. *Geology* **41**, 315–318 (2013).
33. Miller, K.G. *et al.*, Cenozoic sea-level and cryospheric evolution from deep-sea geochemical and continental margin records. *Sci. Adv.* **6**, eaaz1346 (2020)
34. Guo, Z. *et al.* Onset of Asian desertification by 22 Myr ago inferred from loess deposits in China. *Nature* **416**, 159–163 (2002).
35. Sun, X. & Wang, P. How old is the Asian monsoon system?—Palaeobotanical records from China. *Palaeogeogr. Palaeoclimatol. Palaeoecol.* **222**, 181–222 (2005).
36. Farnsworth, A. *et al.* Past East Asian monsoon evolution controlled by paleogeography, not CO2. *Sci. Adv.* **5**, eaax1697 (2019).
37. Spicer, R. *et al.* Paleogene monsoons across India and South China: Drivers of biotic change. *Gondwana Research* **49**, 350–363 (2017).
38. Clift, P.D. *et al.* Correlation of Himalayan exhumation rates and Asian monsoon intensity. *Nat. Geosci.* **1**, 875–880 (2008).

390
391

Methods

Model General Description

The IPSL-CM5A2[25] Earth System Model (ESM) is an updated version of the IPSL-CM5A-LR model ESM[39] . This version benefits from new numerical developments enhancing computational performance, which makes it suitable for deep-time paleoclimate simulations. The model is composed of the atmosphere model LMDz5A[40], the land surface and vegetation model ORCHIDEE[41] and the ocean model NEMO_v3.6[42] that includes an ocean dynamics model (OPA), a thermodynamic-dynamic sea-ice model (LIM2)[43] and a biogeochemistry model (PISCES-v2)[26]. The ocean model grid has a nominal horizontal resolution of 2° by 2° refined up to 0.5° in the equatorial region and 31 vertical levels, whose thickness varies from 10 m near the surface to 500 m at the bottom. The atmosphere grid has a nominal horizontal resolution of 3.75° in longitude by 1.9° in latitude with 39 irregularly distributed vertical levels. Model components are fully described in refs. 25,39. IPSL-CM5A2 has been used for several paleoclimatic studies[44,45], including work focused on the Asian Monsoons[31], and is part of the deep-time Model Intercomparison Projects focused on the Pliocene (PlioMIP2)[27], the mid-Miocene (MioMIP)[46] and the early Eocene (DeepMIP)[47]. Detailed evaluation of the model performance at simulating modern Asian monsoons can be found in ref. 31. General atmospheric circulation over the Asian region and specific characteristics of the South Asian monsoon are correctly simulated by IPSL-CM5A2. Room for improvement exists in the temporality and intensity of the South Asian monsoon as the monsoon onset lags by

414 one month compare to observation and the rainfall intensity during summer over low
415 elevation area is slightly underestimated (Extended Data Figure 7a).

416 **Adaptation of the PISCES model for deep-time studies**

417 The PISCES model simulates the biogeochemical cycles of carbon and main nutrients
418 and lower trophic levels of the marine ecosystem[26]. It includes the representation of 2
419 types of phytoplankton (nanophytoplankton and diatoms) and 2 types of zooplankton
420 functional types and five limiting nutrients (phosphate, nitrate, iron, ammonium and
421 silicate). Phytoplankton growth is limited by the availability of nutrients and light, and water
422 temperature. PISCES also simulates two size classes of particulate organic carbon (small
423 and large) that differ by their sinking rates, as well as the semi-labile dissolved organic
424 matter, dissolved inorganic carbon, alkalinity and dissolved oxygen. A complete
425 description of model parameterizations and evaluation is found in ref. 26. PISCES has
426 been widely used for studying the relationship between marine productivity and global
427 climate[48,49], including paleoclimates[50-53]. In particular, PISCES has also been employed
428 to investigate the relationship between the Indian Monsoon and productivity in the
429 Western Arabian Sea during the Quaternary[53] as well as the impact of ocean physics and
430 dynamics on productivity in the tropical Indian ocean[29]. The overall productivity in the
431 Arabian Sea is correctly simulated[54] though with weaker values compared to observations
432 owing to the weaker Somali jet, which in turn, impacts the coastal upwelling extent and
433 intensity. The absence of meso-scale dynamics due to the moderate ocean resolution
434 also explains some differences between modeled productivity patterns and
435 observations[54]. Despite those well-known biases, the model depicts a realistic

representation of the physical mechanisms driving productivity, and the seasonality of productivity blooms is well simulated[53].

For this study, we have updated the scheme employed to compute the river supply of nutrients and other elements because the paleogeography is significantly different from present-day[55]. In the original version, elements' delivery is fixed and uses results from the Global Erosion Model[56] for DIC and alkalinity or is taken from the GLOBAL-NEWS2 data sets[57] for other elements. Here, the riverine nutrient input to the ocean is calculated as the simulated model runoff times the riverine concentration for each element. As such, the element supply to the ocean is consistent with the Miocene paleogeography and simulated continental runoff. We keep the riverine concentration in elements across the globe constant because there is no simple way of determining how element concentrations might have varied according to local soil composition, vegetation and climate. More importantly, this concentration is adjusted so that the total annual global amount in each supplied element is conserved between the fixed modern supply and the runoff-dependent supply. By doing that, our simulations are designed to isolate and to quantify the effect of ocean dynamics on primary productivity.

Baseline boundary conditions

Late and early Miocene paleogeographies are shown in Extended Data Figure 1. The late Miocene paleogeography is based on the PRISM4[27] reconstruction used in PlioMIP2 [58] (available on the following link : https://geology.er.ugs.gov/egpsc/prism/4_data.html) with additional manual corrections.

The position of the continents is therefore close to present-day. The elevation of mountains belts (including HTP region) is similar to present-day. Major differences include the removal of Hudson Bay and the closure of Bering Strait[27]. The Australian continent is shifted southward to account for its northward migration throughout the Cenozoic[59] and the Sunda shelf has been partly emerged[60]. The early Miocene paleogeography is taken from the recent study of Poblete et al. (2020)[28]. Most of the mountain belts have lower elevation compared to the late Miocene paleogeography to account for major phases of uplift recorded during the late Neogene. In addition, the tip of India is located closer to the equator. The Neo-Tethys seaway is kept closed by a land-bridge (Gomphotherium landbridge[61]) so there is no water mass exchange between Indian and Atlantic Oceans at low latitudes in the early Miocene paleogeography. Another major feature is the existence of a large Peri-Tethys Sea, which covers a substantial part of the European and Asian continents[61]. In the absence of global vegetation reconstructions for both the early and the late Miocene, we use a conservative approach by imposing idealized vegetation with a latitudinal distribution in the two configurations as already done in refs. 31,44. Though vegetation may potentially alter local atmospheric dynamics, the latest research suggests that the large-scale pattern of atmosphere-ocean circulation in the tropical Indian Ocean is mostly driven by SSTs gradients[17]. In order to tease apart the effect of paleogeography alone, the simulations are run with a prescribed atmospheric pCO_2 concentration of 560 ppm whereas other greenhouse gases are set at their pre-industrial values. The solar constant is set at 1364.3 $W.m^{-2}$ for LM and 1362.92 $W.m^{-2}$ for EM and orbital parameters are kept at modern values.

Sensitivity experiments

In addition to simulations performed with baseline configurations (i.e. EM and LM), we investigate the sensitivity of the Arabian Sea atmosphere-ocean dynamics and of the South Asian monsoon patterns to regional changes in topography. These sensitivity experiments consist of altering the topography of either the Anatolian-Iranian Orogen (AIO), the Eastern Arabian Peninsula (EAP), the East African Highlands (EAH) or the Himalayan Tibetan Plateau (HTP), and are either performed with the late or early Miocene baseline paleogeographies (Extended Data Table 1 and Extended Data Figure 3). We focused on the major regional changes in topography and land-sea distribution around the Indian Ocean basin that have been suggested in the literature to drive first-order changes in large-scale monsoon dynamics. These sensitivity experiments integrate existing uncertainties in paleogeographic reconstructions because the intricate uplift history of Asian, East African and Middle-East orogens is still a subject of active research.

Thermochronology and paleoaltimetry studies indicate that the Central Tibetan Plateau had reached high elevations (> 4,000 m) by the early Miocene[12,62-66]. The Himalayan mountain range attained high elevations similar to present day in the late early Miocene (~ 15 Ma) [12,13,66], a configuration we test in the EM-HTP configuration (Extended Data Figure 3g). Some studies also suggest a configuration in which the Himalayan topography is higher than today, possibly sustained by slab break off, to explain rainfall intensification during the early to middle Miocene[66]. We test this scenario in the EM-Him simulation (Extended Data Figure 3h).

Uplift in East Africa initiated in the Eocene/Oligocene with the doming in Ethiopia and Kenya[67]. This episode corresponds to the establishment of long-wavelength topography associated with mantle dynamics (see ref[68] for a review). In Ethiopia, traps volcanism occurred during the Early Oligocene[68] leading to the formation of ~1km thick continental flood basalts covering pre-existing topography. The Ethiopian plateau can be possibly as high as 2500-3000 m in place before the middle Miocene[69-72]. East African Highlands (East African Rift and Afar-Yemen-Arabia Plateau) then underwent continuous uplift during the Neogene[69,72] owing to rifting processes : beginning in Ethiopia during the middle Miocene and then propagating southwards[68]. Topography in the central Kenya region was probably high in the middle Miocene (above 1,400m elevation before 13.5 Ma)[72]. We test the effect of uplifting topography in East Africa in the EM-EAH configuration, in which we prescribed the LM EAH topography onto the EM baseline geography (Extended Data Table 1 and Extended Data Figure 3f). The impact of late Miocene uplift of rift-associated topography has also been tested on the LM-NoAIO geography by capping the elevation at 1,500 meters (an altitude likely reached before the middle Miocene) but maintaining the morphology of the large-scale topography (Extended Data Figure 3d ; LM-EAHR). This latter sensitivity experiment have results similar to LM-NoAIO, which suggest that late Miocene uplift related the EAH rift activity have had little impact on the atmospheric circulation and upwelling. Results on Figure 4d-e however shows that rainfall in the SAM region are sensitive to African topography[20-21] a question that should be further explored.

In the Middle-East, the Iranian Plateau and Anatolian topography rise at some point after 17 Ma due to the long-term collision of the Arabian and Eurasian Plates[32], most likely during the late Miocene[73,74], which is later than the settlement of high topography in East-Africa[67-72] and HTP regions[12,62-66] . We therefore run an experiment in which we decrease the height of regional topography by half on the LM configuration (LM-NoAIO, Extended Figure 3b).

The Tethyan Seaway also closed permanently around 14 Ma[61,75] and continental area replaces marine environments in the Eastern Arabian Peninsula[61] due both to tectonics evolution of the Middle East[32] and to the sea level drop following Antarctic ice-sheet expansion during the Middle Miocene Climate Transition (up to 80 m[33]) . Existing paleogeographic reconstructions shows the Eastern Arabian Peninsula as partly submerged during the Burdigalian (early Miocene) and emerged in the late Miocene[61]. Because of its flatness, the north-eastern part of Arabian Peninsula is highly sensitive to sea level fall and we hypothesize that the sea level drop during the MMCT could have led to emergence of previously submerged land surface. Based on this hypothesis, the effect of changes in land-sea extension over the Eastern Arabian Peninsula is tested in the LM-NoEAP configuration (Extended Data Figure 3c). Other details of regional paleogeography, such as narrow mountain belts (e.g. the Western Ghats in India)) have not been considered in the present study. Although these small-scale features influence rainfall and wind patterns at the local scale[76,77] they do not represent first order controls on the large-scale, trans-oceanic, monsoon dynamics[17].

In addition to sensitivity experiments on topography and land-sea distribution, we also assess the impact of coeval global climatic changes occurring during the late middle Miocene using sensitivity simulations with an expanded Antarctic ice-sheet[78,79] or a lower CO_2 concentration[80] (Extended Data Table 1).

Experimental design

IPSLCM5A2 simulations are initialized with idealized ocean conditions (except EM-Him and EM-HTP that restart from EM, Extended Data Table 1) consisting of a latitudinally-varying, zonally symmetric, temperature distribution and a constant salinity distribution[81]

$T(^{\circ}C) = (1000 - z)/1000 * 20 \cos(lat) + 10$ for $z <= 1000$ m

$T(^{\circ}C) = 10$ for $z > 1000$ m

S (PSU) = 34.7

Each simulation is run for more than 2,500 years, until the deep ocean reaches a quasi-equilibrium with only small residual trends of less than 0.1°C per century (Extended Data Figure 9). Our simulations are analyzed and discussed using climatological averages calculated over the last 100 model years. In a second step, we use the climatology corresponding to each IPSLCM5A2 simulation to force the offline version of PISCES in order to increase the spin-up time of marine biogeochemistry[82]. In each offline PISCES simulation, the prescribed nutrient concentration in rivers is adjusted to the total runoff flux to conserve the total modern global amount of nutrients delivered to the ocean. The

563 global amount of nutrients is thus fixed to its modern value, which enable us to attribute
564 modifications in primary productivity to changes in ocean dynamics.

565 **Model evaluation**

566 We provide here a basic assessment of the model performance compared to available
567 Miocene SST estimates (Extended Data Figure 9b-c, compilation from ref. 45 and
568 reference therein) and note that a more detailed investigation can be found in ref. 45 that
569 is part of the MioMIP project. The model-data comparison shows an overall good fit for
570 both EM and LM simulations (Extended Data Figure 9b-c), in particular in the tropical to
571 mid-latitude domains, where our study is focused (northern Indian Ocean and South
572 Asia). There are some discrepancies at higher latitudes in the Atlantic Ocean that are
573 systematic characteristics of multi-model Miocene simulations because models fail to
574 reproduce the polar amplification and reduced equator-pole SST gradient inferred from
575 the data record[46].

576 **Data Availability**

577 All model outputs used in this study are available as NetCDF file on the following Zenodo
578 repository[85] : https://doi.org/10.5281/zenodo.5727042. The early Miocene
579 paleogeographic reconstructions[28] is also available on the Paleoenvironment map
580 website (https://map.paleoenvironment.eu). The repository also contains paleogeography
581 grids used for the simulations. Colored figures in this paper were made with perceptually
582 uniform, color-vision-deficiency-friendly scientific color maps, developed and distributed
583 by Fabio Crameri[86]

584

Code availability

LMDZ, XIOS, NEMO and ORCHIDEE are released under the terms of the CeCILL license. OASIS-MCT is released under the terms of the Lesser GNU General Public License (LGPL). IPSL-CM5A2 source code is publicly available through svn, with the following commands line :svn co http://forge.ipsl.jussieu.fr/igcmg/svn/modipsl/branches/publications/IPSLCM5A2.1_1119 2019 modipsl ; cd modipsl/util ; ./model IPSLCM5A2.1

The mod.def file provides information regarding the different revisions used, namely : - NEMOGCM branch nemo_v3_6_STABLE revision 6665
- XIOS2 branchs/xios-2.5 revision 1763
- IOIPSL/src svn tags/v2_2_2

- LMDZ5 branches/IPSLCM5A2.1 rev 3591
- branches/publications/ORCHIDEE_IPSLCM5A2.1.r5307 rev 6336 - OASIS3-MCT 2.0_branch (rev 4775 IPSL server)

The login/password combination requested at first use to download the ORCHIDEE component is anonymous/anonymous. We recommend that you refer to the project website: http://forge.ipsl.jussieu.fr/igcmg_doc/wiki/Doc/Config/IPSLCM5A2 (last access: 7 February, 2022) for a proper installation and compilation of the environment.

Adaptation of PISCES model used in the study have been archived on the following Zenodo repository : 10.5281/zenodo.5727042) in addition with information on how to include the updates in the reference code of PISCES.

Analysis and graphics from this paper have been done using open source tools. PyFerret is a product of NOAA's Pacific Marine Environmental Laboratory (information is available at http://ferret.pmel.noaa.gov/Ferret/). Information on NCL[87] is available at https://www.ncl.ucar.edu. Information on Generic Mapping Tool[88] is available at https://www.generic-mapping-tools.org.

Methods reference

39. Dufresne, JL. *et al.,* Climate change projections using the IPSL-CM5 earth system model: from CMIP3 to CMIP5. *Clim. Dyn.* **40**, 2123–2165 (2013).
40. Hourdin**,** F. *et al.,* Impact of the LMDz atmospheric grid configuration on the climate and sensitivity of the IPSL-CM5A coupled model. *Clim.Dyn.***40**, 2167–2192 (2013).
41. Krinner, G. *et al.,* A dynamic global vegetation model for studies of the coupled atmosphere-biosphere system. *Glob. Biogeochem. Cycles* **19** (2005).
42. Madec, G. NEMO ocean engine. note du pôle de modélisation de l'institut Pierre-Simon Laplace **27**, 386 pp (2016).
43. Fichefet, T. & Maqueda, M. M. Sensitivity of a global sea ice model to the treatment of ice thermodynamics and dynamics. *J. Geophys. Res. Ocean.* **102**, 12609–12646 (1997).

44. Laugié, M. *et al.*, Stripping back the modern to reveal the Cenomanian–Turonian climate and temperature gradient underneath. *Clim. Past* **16**, 953–971 (2020).
45. Toumoulin, A. *et al.*, Quantifying the effect of the Drake passage opening on the eocene ocean. *Paleoceanogr. Paleoclimatology* **35**, e2020PA003889 (2020).
46. Burls, N. B. *et al.*, Simulating Miocene warmth: insights from an opportunistic multi model ensemble 1 (MioMIP1). *Paleoceanogr. Paleoclimatology **36,*** e2020PA004054 (2021).
47. Lunt, D. J. *et al.,* DeepMIP: Model intercomparison of early Eocene climatic optimum (EECO) large-scale climate features and comparison with proxy data. *Clim. Past **17,*** 203-227 (2021).
48. Bopp, L. *et al.,* Multiple stressors of ocean ecosystems in the 21st century: projections with CMIP5 models. *Biogeosciences* **10**, 6225–6245 (2013).
49. Ladant, J-B., Donnadieu, Y., Bopp, L., Lear, C. H. & Wilson, P. A. Meridional contrasts in productivity changes driven by the opening of Drake passage. *Paleoceanogr. Paleoclimatology* **33**, 302–317 (2018).
50. Bopp, L., Kohfeld, K. E., Le Quéré, C. & Aumont, O. Dust impact on marine biota and atmospheric CO_2 during glacial periods. *Paleoceanography* **18** (2003).
51. Tagliabue, A. *et al.*, Quantifying the roles of ocean circulation and biogeochemistry in governing ocean carbon-13 and atmospheric carbon dioxide at the last glacial maximum. *Clim. Past* **5**, 695–706 (2009).
52. Bopp, L., Resplandy, L., Untersee, A., Le Mezo, P. & Kageyama, M. Ocean (de) oxygenation from the last glacial maximum to the twenty-first century:

insights from earth system models. *Philos. Transactions Royal Soc. A: Math. Phys. Eng. Sci.* **375**, 20160323 (2017).

53. Le Mézo, P., Beaufort, L., Bopp, L., Braconnot, P. & Kageyama, M. From monsoon to marine productivity in the arabian sea: insights from glacial and interglacial climates. *Clim. Past* **13**, 759 (2017).

54. Resplandy, L., Lévy, M., Madec, G., Pous, S., Aumont, O. & Kumar,D. Contribution of mesoscale processes to nutrient budgets in the Arabian sea. *J. Geophys. Res. Ocean.* **116** (2011).

55. Laugié, M., *et al.* Exploring the Impact of Cenomanian Paleogeography and Marine Gateways on Oceanic Oxygen. Paleoceanogr. Paleoclimatology **36,** e2020PA004202 (2021).

56. Ludwig, W., Probst, J-L. & Kempe, S. Predicting the oceanic input of organic carbon by continental erosion. *Glob. Biogeochem. Cycles* **10**, 23–41 (1996).

57. Mayorga, E. *et al.*, Global nutrient export from watersheds 2 (NEWS 2): model development and implementation. *Environ. Model. & Softw.* **25**, 837–853 (2010).

58. Haywood, A. M. *et al.,* A return to large-scale features of Pliocene climate: the Pliocene Model Intercomparison Project phase 2. Clim. Past 6, 2095-2123 (2020).

59. Torsvik, T. H., Müller, R. D., Van der Voo, R., Steinberger, B. & Gaina, C. Global plate motion frames: toward a unified model. *Rev. geophysics* **46** (2008).

60. Hall, R. Sundaland and Wallacea: geology, plate tectonics and palaeogeography. *Biotic evolution environmental change Southeast Asia* **32**, 78 (2012).

669 61. Rögl, F. Mediterranean and Paratethys. Facts and hypotheses of an Oligocene to
670 Miocene paleogeography (short overview). *Geol. Carpathica* **50**, 339–349 (1999).
671 62. Fang, X. *et al.*, Revised chronology of central Tibet uplift (Lunpola basin). *Sci.*
672 *Adv.* **6**, eaba7298 (2020).
673 63. Botsyun, S. *et al.,* Revised paleoaltimetry data show low Tibetan plateau
674 elevation during the Eocene. *Science* **363** (2019).
675 64. Quade, J., Breecker, D. O., Daëron, M. & Eiler, J. The paleoaltimetry of Tibet:
676 An isotopic perspective. *Am. J. Sci.* **311**, 77–115 (2011).
677 65. Wang, W. *et al.*, Expansion of the Tibetan plateau during the Neogene. *Nat.*
678 *Commun.* **8**, 1–12 (2017).
679 66. Webb, A. A. G. *et al.,* The Himalaya in 3D: Slab dynamics controlled mountain
680 building and monsoon intensification. *Lithosphere* **9**, 637–651 (2017).
681 67. de Gouveia SV, Besse J, de Lamotte DF, Greff-Lefftz M, Lescanne M, Gueydan
682 F, et F. Leparmentier. Evidence of hotspot paths below Arabia and the Horn of
683 Africa and consequences on the Red Sea opening. Earth and Planetary Science
684 Letters. (2018), 487, 210-20.
685 68. Couvreur T. L.P. *et al.* Tectonic, climate and the diversification of the tropical
686 African terrestrial flora and fauna. Bio. Rev. **96**, 16-51(2020).
687 69. Sembroni et *al.* Long-term, deep-mantle support of the Ethiopia-Yemen Plateau,
688 *Tectonic*s, **35**, 469-488 (2016)
689 70. Faccenna, C. *et al.,* Role of dynamic topography in sustaining the Nile river over
690 30 million years. *Nat. Geosci* **12**, 1012–1017 (2019).

71. Pik, R., Marty, B., Carignan, J. Yirgu, G. & Ayalew, T. Timing of East African Rift development in southern Ethiopia; implication for mantle plume activity and evolution of topography. *Geology*, **36**,167-170 (2008)
72. Wichura, H., Bousquet R., Oberhänsli, R., Strecker, M. R. & Trauth, M.H., Evidence for middle Miocene uplfit of East African Plateau. Geology **38**, 543-546 (2010).
73. François, T. *et al.*, Cenozoic exhumation of the internal Zagros: first constraints from low-temperature thermochronology and implications for the build-up of the Iranian plateau. *Lithos* **206-207**, 100–112 (2014).
74. Austermann, J. & Iaffaldano, G. The role of the zagros orogeny in slowing down Arabia-Zurasia convergence since 5 Ma. *Tectonics* **32**, 351–363 (2013).
75. Bialik, O. M., Frank, M., Betzler, C., Zammit, R. & Waldmann, N. D. Two-step closure of the Miocene Indian Ocean Gateway to the Mediterranean. *Sci. Reports* **9**, 1–10 (2019).
76. Xie, S. P., Xu, H., Saji, N. H., Wang, Y. & Liu, W.T. et al. Role of narrow mountains in large-scale organization of Asian monsoon convection. *Journal of climate*, ***19***, 3420-3429 (2006).
77. Sijikumar, S., John, L. & Manjusha, K. Sensitivity study on the role of Western Ghats in simulating the Asian summer monsoon characteristics. *Meteorology and Atmospheric Physics*, **120**, 53-60 (2013).

78. Leutert, T.J., Auderset, A., Martínez-García, A., Modestou, S. & Meckler, A. N. Coupled southern ocean cooling and Antarctic ice sheet expansion during the middle Miocene. *Nat. Geosci.* **13**, 634–639 (2020).
79. Gasson, E., DeConto, R. M., Pollard, D. & Levy, R. H. Dynamic Antarctic ice sheet during the early to mid-Miocene. *Proc. Natl. Acad. Sci.* **113**, 3459–3464 (2016).
80. Foster, G. L., Royer, D. L. & Lunt, D. J. Future climate forcing potentially without precedent in the last 420 million years. *Nat. Commun.* **8**, 14845 (2017).
81. Lunt, D.J. *et al.*, The DeepMIP contribution to PMIP4: experimental design for model simulations of the EECO, PETM, and pre-PETM (version 1.0), *Geosci. Model. Dev.* **10**, 889–901 (2017).
82. Séférian, R. *et al.,* Inconsistent strategies to spin up models in CMIP5: implications for ocean biogeochemical model performance assessment. *Geosci. Model. Dev.* **9**, 1827–1851 (2016).
83. Huffman, G. J., Adler, R. F., Bolvin, D.T. & Gu, G. Improving the global precipitation record: GPCP version 2.1. *Geophys. Res. Lett.* **36** (2009).
84. Herbert, T. D. *et al.*, Late Miocene global cooling and the rise of modern ecosystems. *Nat. Geosci.* **9**, 843–847 (2016).
85. Sarr, A-C. (2022). Evolution of Indian Ocean Paleoceanography and South-East Asian Climate during the Miocene in response to change in regional topography [Data set]. Zenodo. https://doi.org/10.5281/zenodo.5727042
86. Crameri, F., Shephard, G. E. & Heron, P. J. The misuse of colour in science communication. *Nat. Commun.* **11**, 1–10 (2020).

87. The NCAR Command Language (version 6.3.0) [Software]. (2015). Boulder Colorado: UCAR/NCAR/CISL/TDD. http://dx.doi.org/10.5065/D6WD3XH5

88. GMT 5**:** Wessel, P., W. H. F. Smith, R. Scharroo, J. Luis, and F. Wobbe, Generic Mapping Tools: Improved Version Released, *EOS Trans. AGU*, 94(45), p. 409–410, 2013. doi:10.1002/2013EO450001.

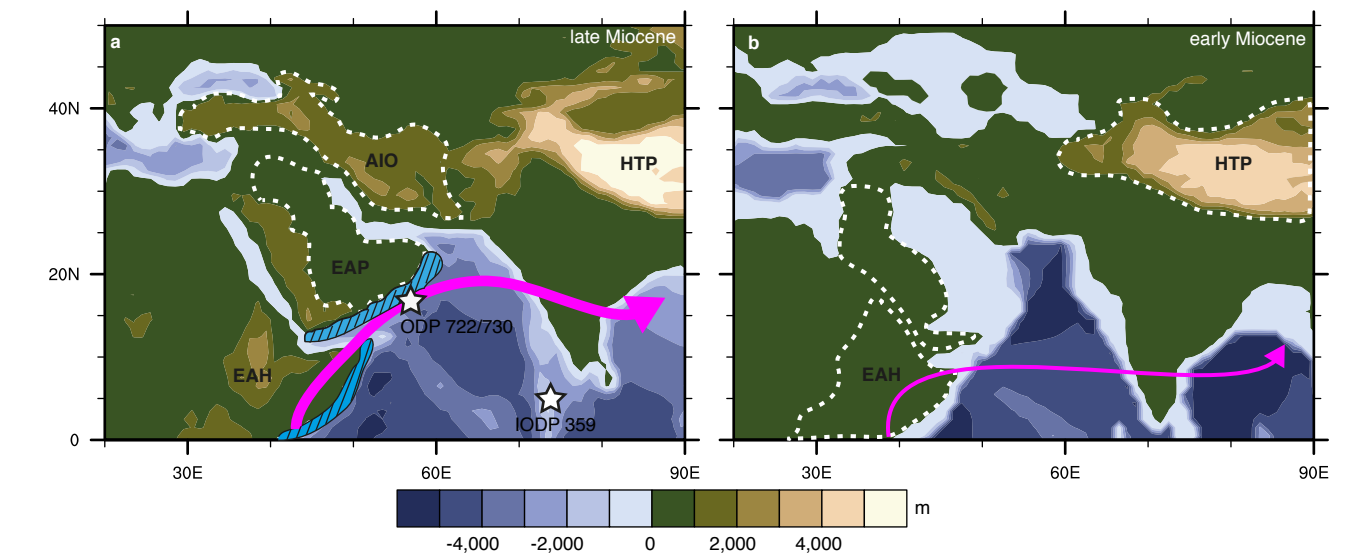
a
late Miocene
b
early Miocene
AIO
HTP
EAP
EAH
ODP 722/730
IODP 359
HTP
EAH
40N
20N
0
30E
60E
90E
30E
60E
90E
m
-4,000
-2,000
0
2,000
4,000

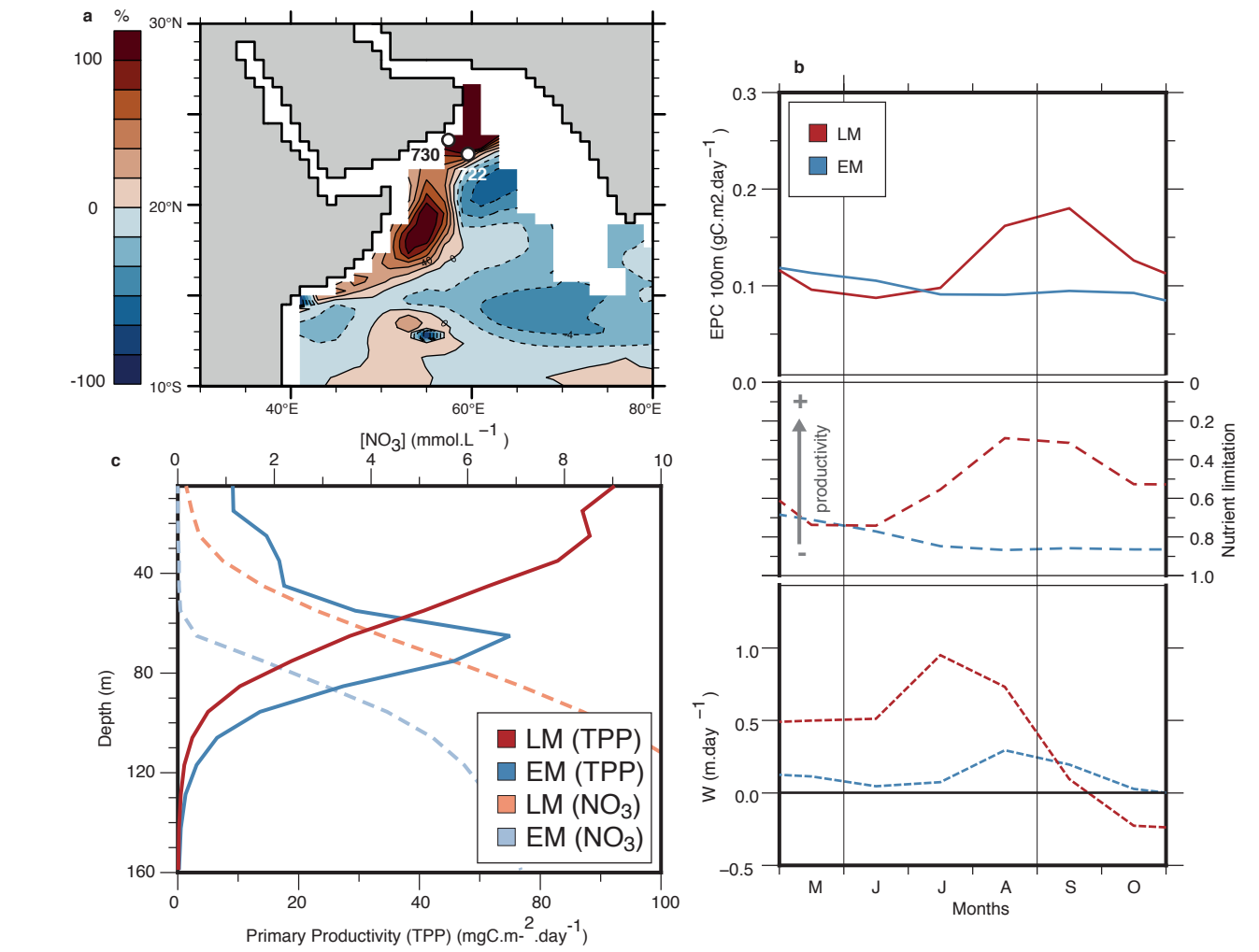
a
%
100
0
-100
30°N
20°N
10°S
40°E
60°E
80°E
730
22
[NO3] (mmol.L −1)
b
LM
EM
EPC 100m (gC.m2.day −1)
0.3
0.2
0.1
0.0
+
productivity
-
0
0.2
0.4
0.6
0.8
1.0
Nutrient limitation
W (m.day −1)
1.0
0.5
0.0
−0.5
M
J
J
A
S
O
Months
c
Depth (m)
0
40
80
120
160
2
4
6
8
10
20
40
80
100
LM (TPP)
EM (TPP)
LM (NO3)
EM (NO3)
Primary Productivity (TPP) (mgC.m-2.day-1)

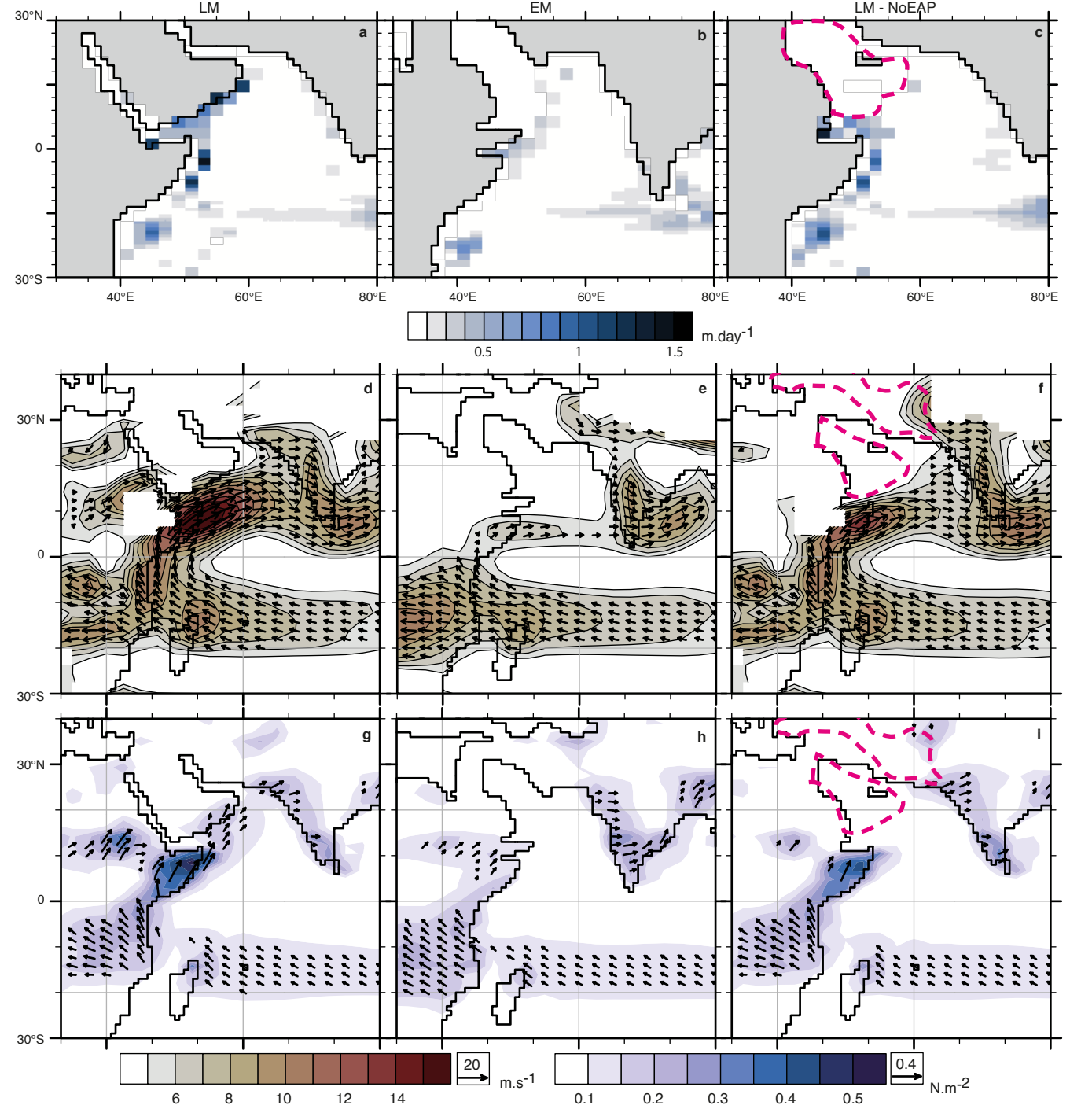
LM
EM
LM - NoEAP
a
b
c
30°N
0
30°S
40°E
60°E
80°E
0.5
1
1.5
m.day-1
d
e
f
g
h
i
6
8
10
12
14
20
m.s-1
0.1
0.2
0.3
0.4
0.5
0.4
N.m-2

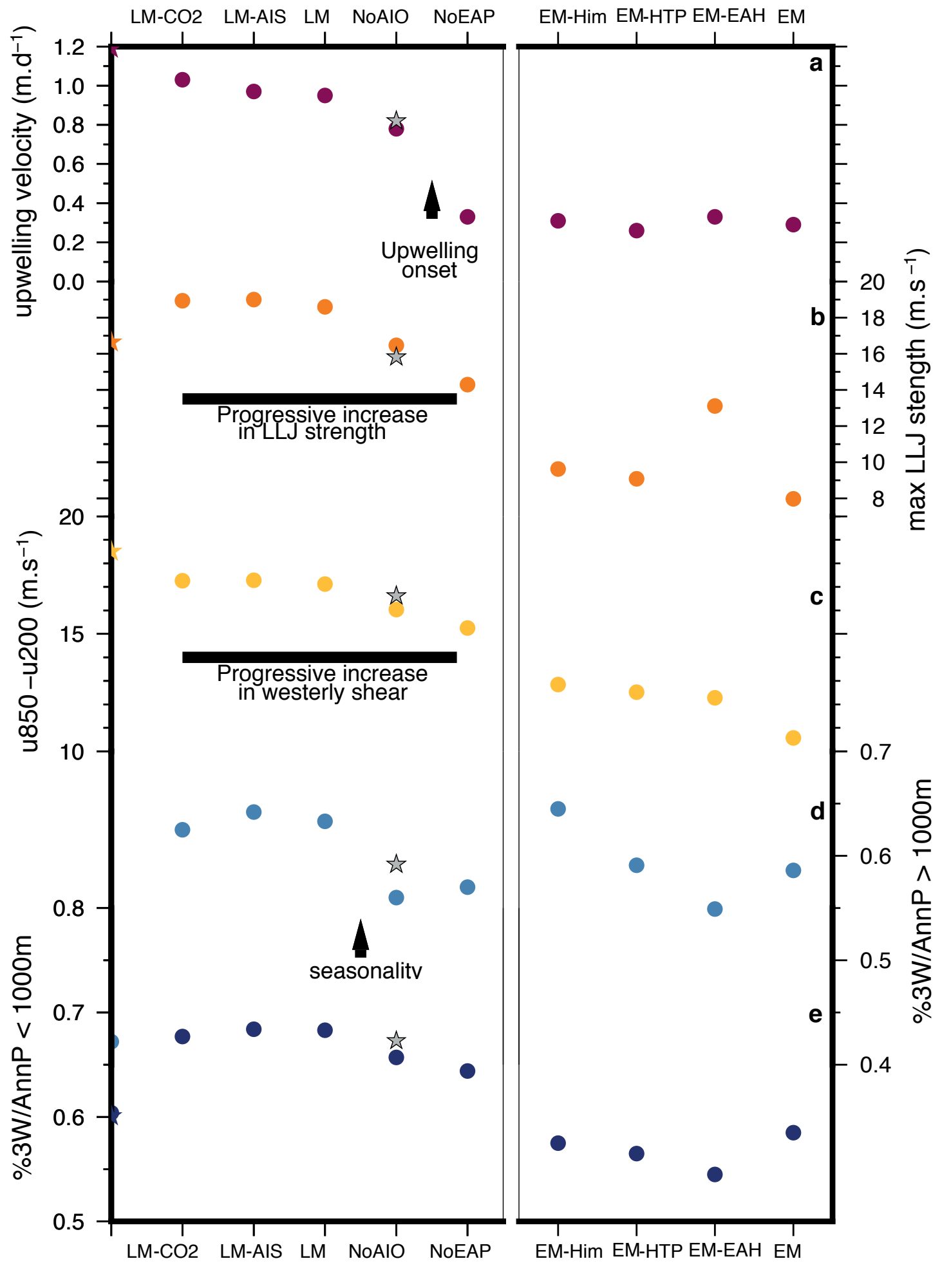
LM-CO2
LM-AIS
LM
NoAIO
NoEAP
EM-Him
EM-HTP
EM-EAH
EM
upwelling velocity (m.d^{-1})
u850–u200 (m.s^{-1})
%3W/AnnP < 1000m
max LLJ stength (m.s^{-1})
%3W/AnnP > 1000m
a
b
c
d
e
Upwelling onset
Progressive increase in LLJ strength
Progressive increase in westerly shear
seasonality

Extended Data Table 1: Simulations performed with IPSL-CM5A2. See Supplementary Figure 1 and 3 for paleogeography maps.

Simulation	pCO_2 (ppm)	Geography	Sensitivity experiments			
			East Africa	HTP	Anatolia-Iran	East Arabian Plate
EM	560	Early Miocene Paleogeography	Low		Early Miocene	
EM-EAH			From LM			
EM-HTP			Low	From LM		
EM-Him			Low	From LM + 20% higher Himalaya		
LM	560	Late Miocene Paleogeography	100%	Late Miocene	100 %	100 %
LM-NoAIO			100%		50 %	100 %
LM-NoEAP			100%		50 %	0 %
LM-NoEAHR			60%		50%	100%
LM-AIS			100%		100 %	100 %
LM-CO2	420		100%		100 %	100 %

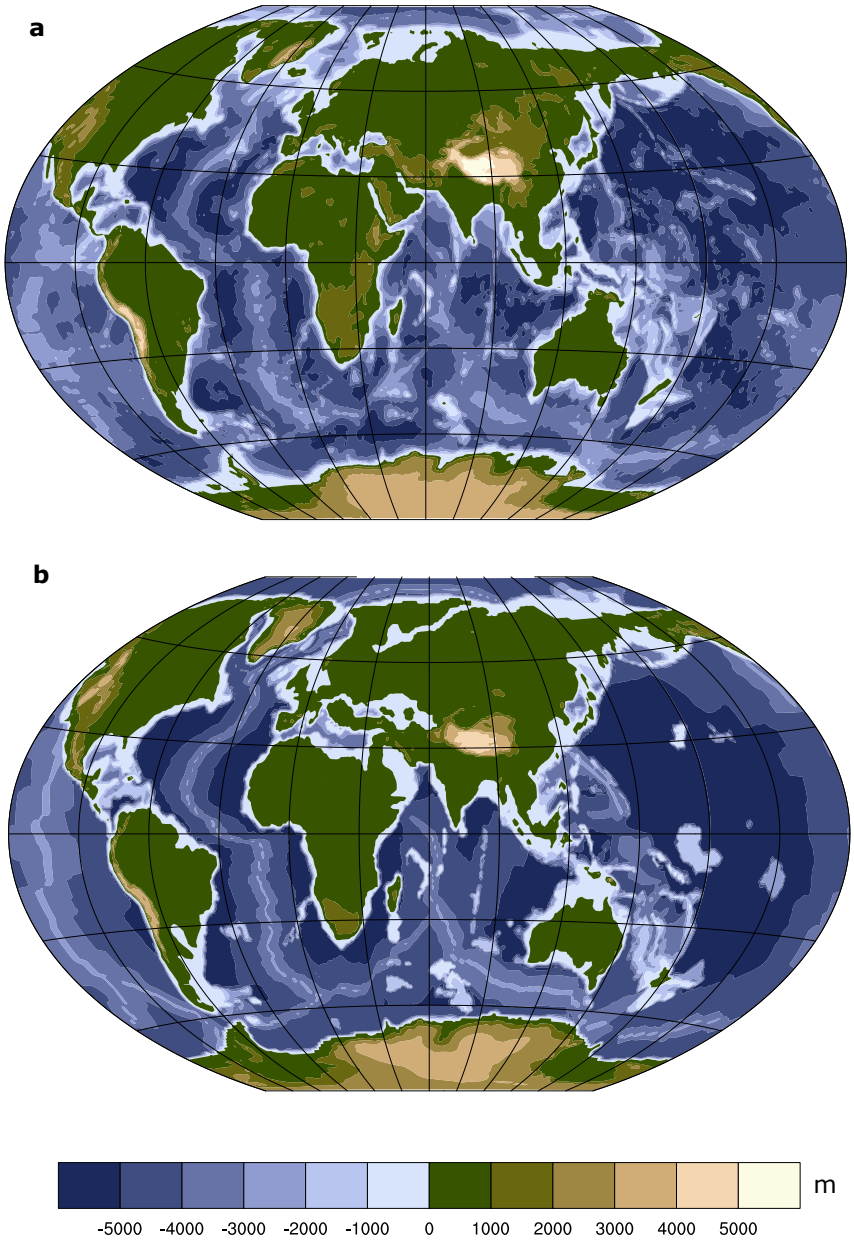

Extended Data Figure 1: Paleogeographic reconstruction used in the reference simulations. a) late Miocene (LM) and b) early Miocene (EM) simulations. Initial bathymetry is more detailed in LM than in EM paleogeography, but the model resolution (2° by 2°) mitigates the difference by smoothing small variations.

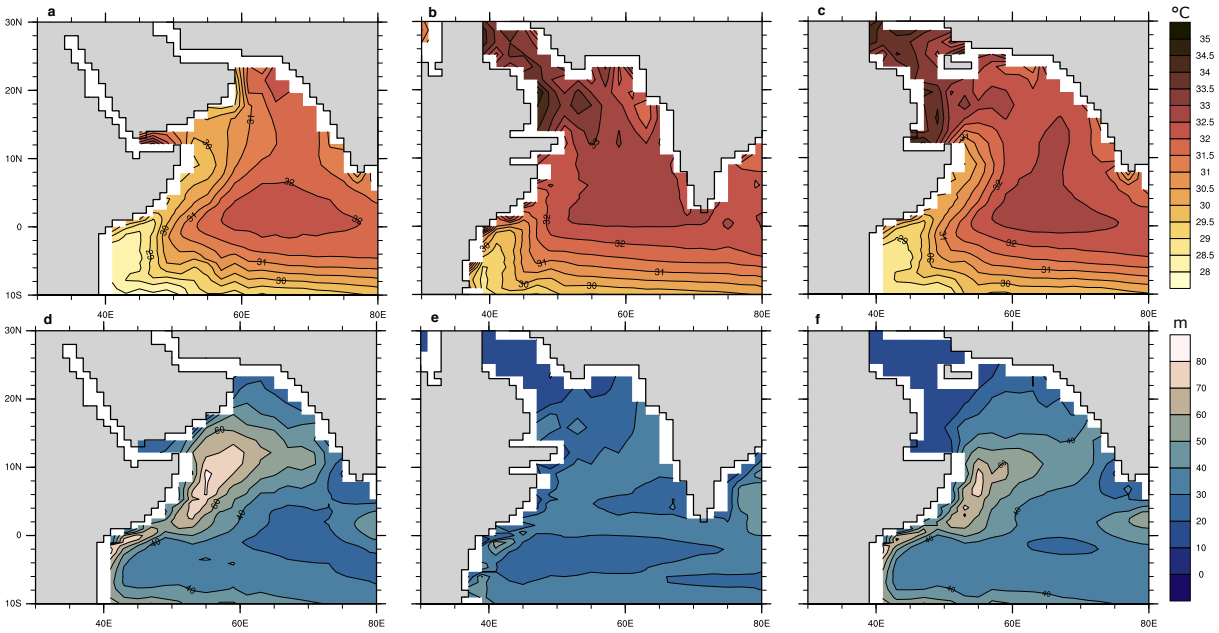

Extended Data Figure 2: Western Indian ocean response to Miocene paleogeographic evolution

Top : Sea surface temperatures (°C) averaged over boreal summer (JAS) ; Bottom : Mixed layer depth average during boreal summer (JAS). (a)(d) late Miocene (LM) and (b)(e) early Miocene (EM) and (c)(f) LM-NoEAP simulations (See Extended Data Tab. 1 and Extended Data Fig. 3). LM-NoEAP is a simulation without the Eastern Arabian Peninsula (EAP), designed to show the influence of Arabian Peninsula immersion on the Somali Jet structure in a LM configuration.

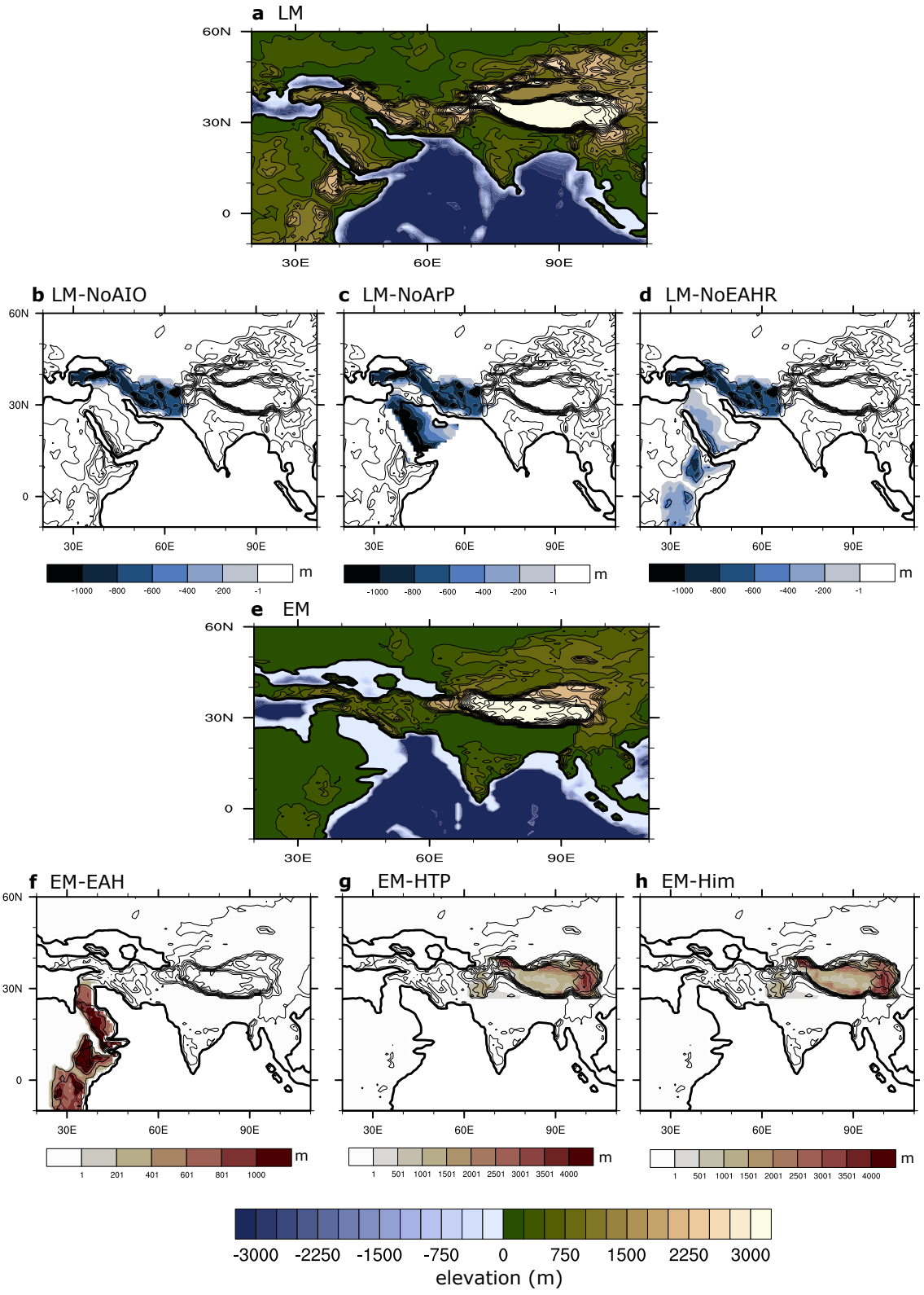

Extended Data Figure 3: Paleogeographic changes used in the sensitivity experiment. Paleogeography surrounding the Indian Ocean in a) the late Miocene (LM) and e) the early Miocene (EM) simulations. Change in paleogeography between sensitivity experiments and the reference simulation (LM and EM) ; b) LM-NoAIO (change in Anatolia-Iran orogen (AIO) topography) ; c) LM-NoEAP (Change in Arabian Peninsula (EAP) land extension) d) LM-NoEAHR (Change in East African Highland (EAH) topography on LM configuration) ; f) EM-EAH (Change in East African Highland topography on EM configuration) ; g) EM-HTP (Change in Himalaya and Tibetan Plateau (HTP) topography) and g) EM-Him (Higher than present-day Himalaya). Contours are drawn every 250 meters for EM and LM simulations and every 500 meters for each sensitivity experiment.

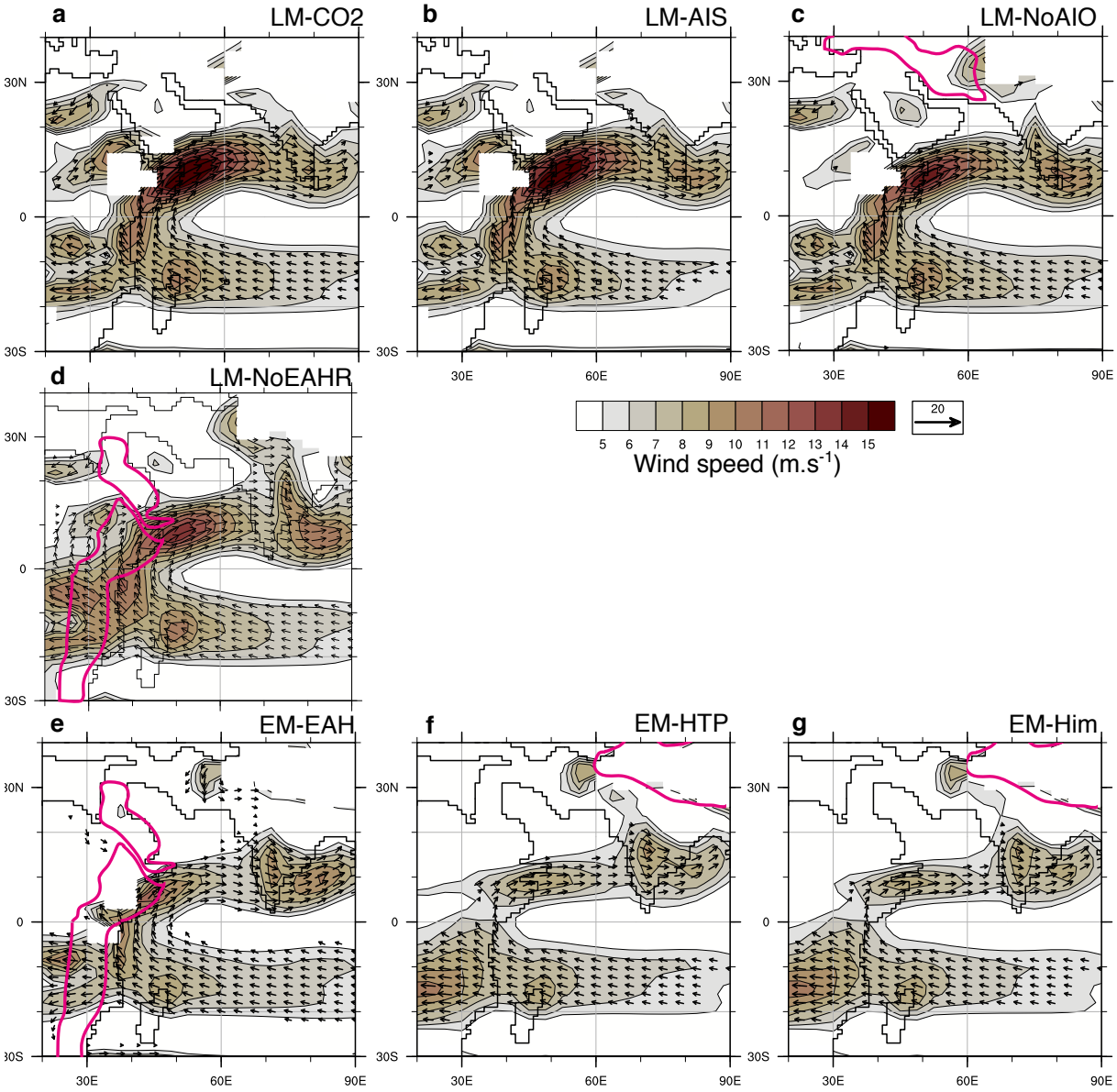

Extended Data Figure 4: Somali Jet response to changes in regional paleogeography. Low level winds (850 hPa) during boreal summer (JJA) for a) late Miocene (LM) with low CO_2 (LM-CO_2); b) LM with Expanded Antarctic Ice Sheet (LM-AIS); c) LM with half present-day Anatolia-Iran topography (LM-NoAIO); d) LM with reduced topography in East African Highlands (LM-noEAHR) ; e) EM with uplifted East African Highlands (EM-EAH); f) EM with fully uplifted HTP region (EM-HTP) and g) EM with higher than present-day Himalaya orography (EM-Him).

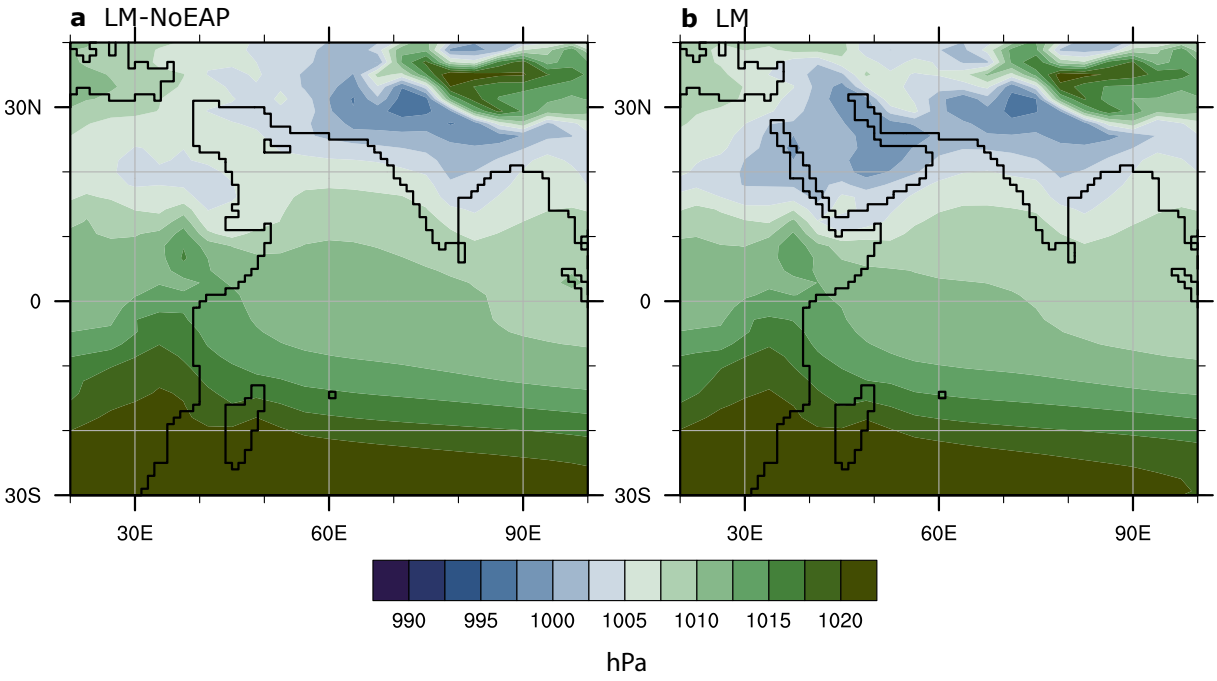

Extended Data Figure 5: Sea level pressure response to Middle Eastern physiographic changes. Mean summer (JJA) sea level pressure (hPa) for a) late Miocene (LM) with partly submerged Eastern Arabian Peninsula (LM-NoEAP) and b) late Miocene baseline simulation.

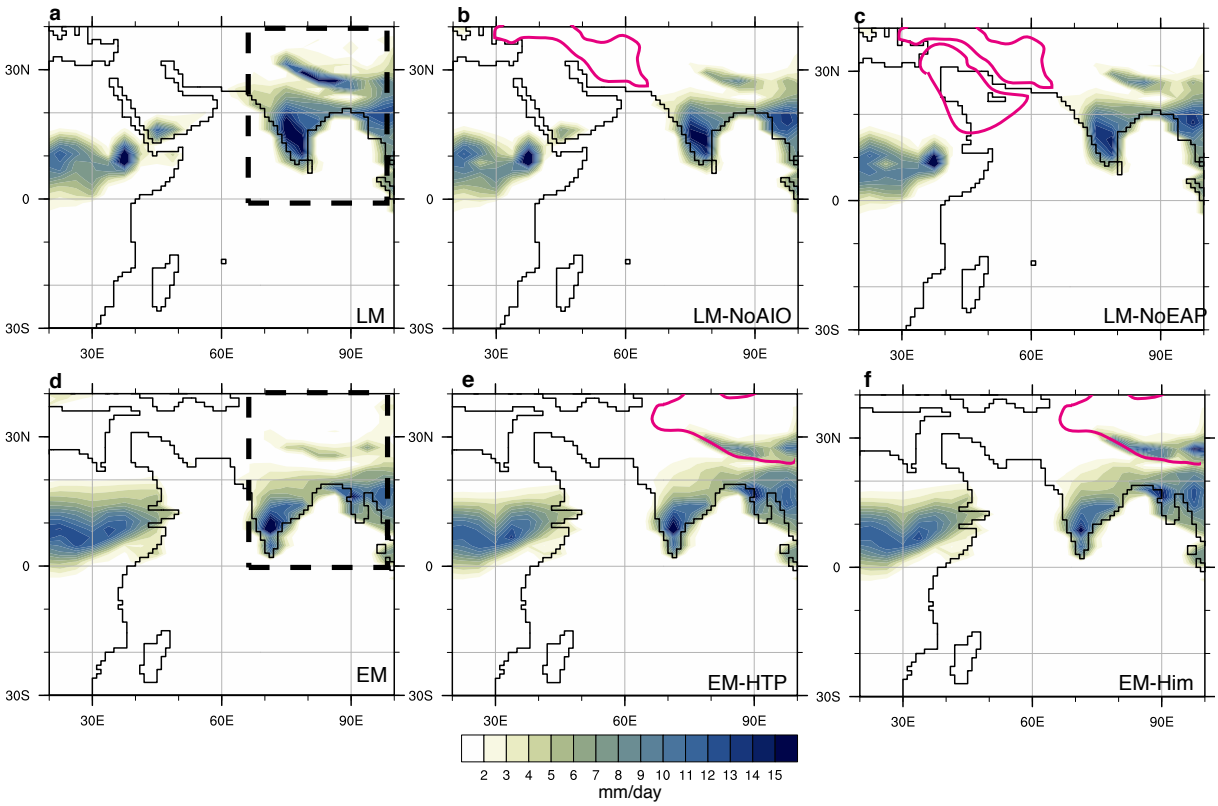

Extended Data Figure 6: Mean summer precipitation response to change in regional physiography. a) late Miocene (LM), b) LM with half present-day Anatolia-Iran topography (LM-AIO), c) LM with partly submerged Eastern Arabian Peninsula (LM-NoEAP) and reduced topography in the Anatolia-Iran region, d) early Miocene, e) EM with fully uplifted HTP region (EM-HTP), f) EM with higher than present-day Himalaya orography (EM-Him). Dashed square indicates the area over which inland precipitation seasonality index (Main text, Figure 4) is computed.

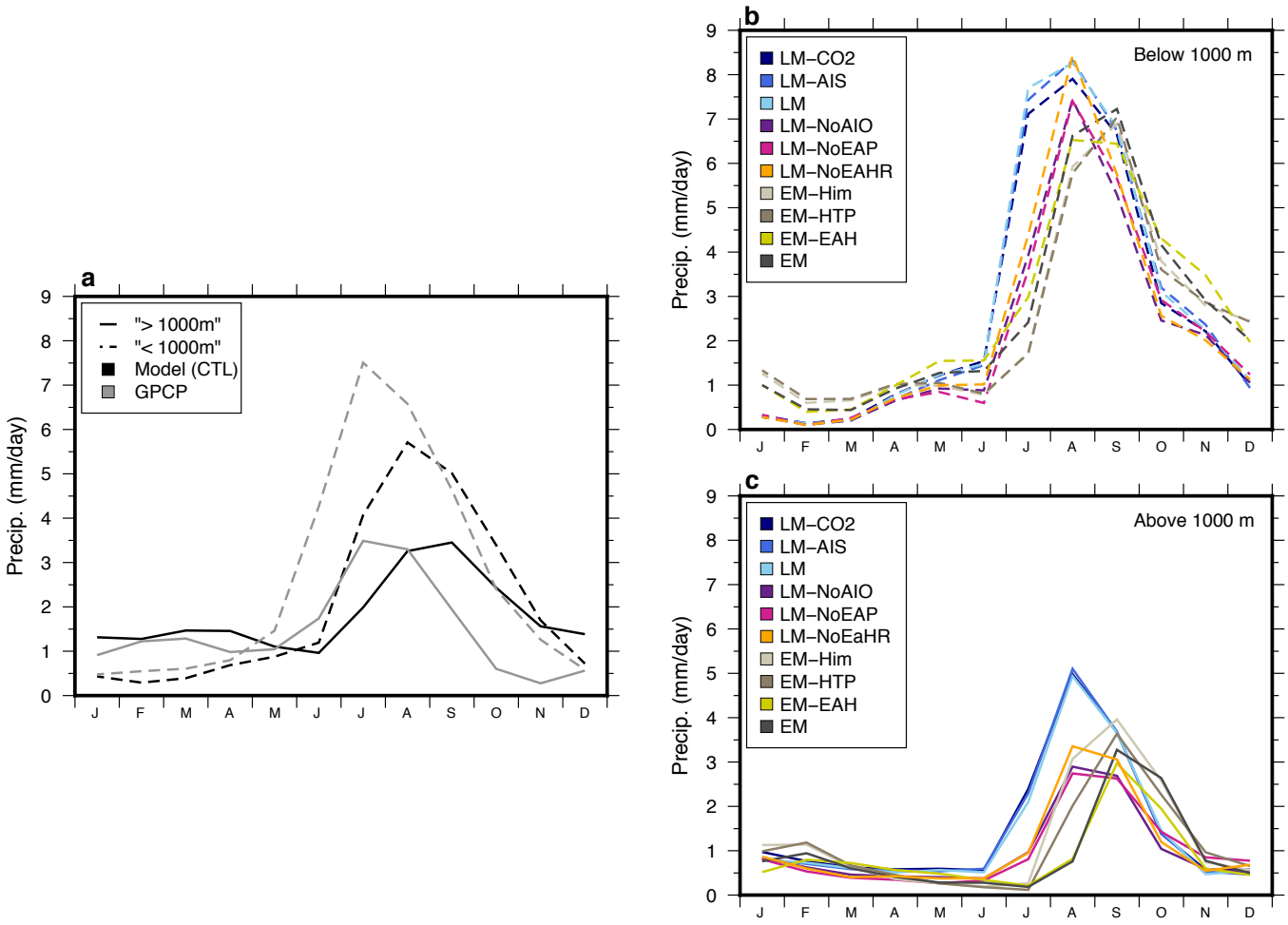

Extended Data Figure 7: Seasonal cycle of precipitation. Precipitation is averaged over [65°E-85°E, 0-35°N]. a) Global Precipitation Climatology Project (GPCP) data[82] and preindustrial simulation[24] (Model), b) Low elevation areas (0-1,000 m) and c) high altitude areas (above 1000m) for early Miocene (EM) and late Miocene (LM) simulations and sensitivity experiments.

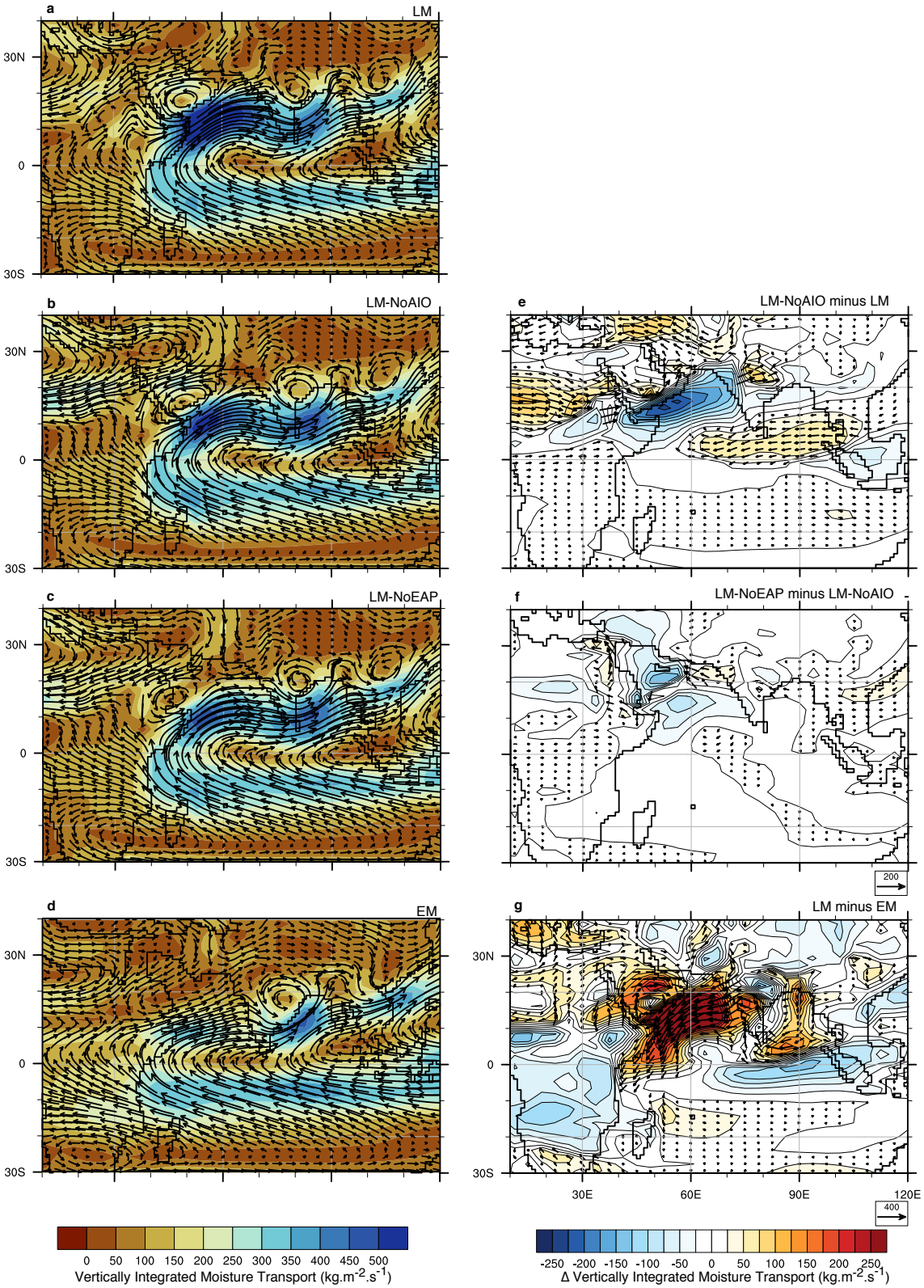

Extended Data Figure 8: Moisture transport response to change in regional physiography. Late summer vertically integrated moisture transport (JJA) a) late Miocene (LM); b) LM-NoAIO; c) LM-NoEAP, d) early Miocene (EM). Change in vertically integrated moisture transport (JJA) in response to e) change in Anatolia-Iran topography (LM-NoAIO vs. LM); f) emersion of the Eastern Arabian Peninsula (LM-NoEAP vs. LM-NoAIO) and g) paleogeographic evolution between the early and the late Miocene (LM vs. EM).

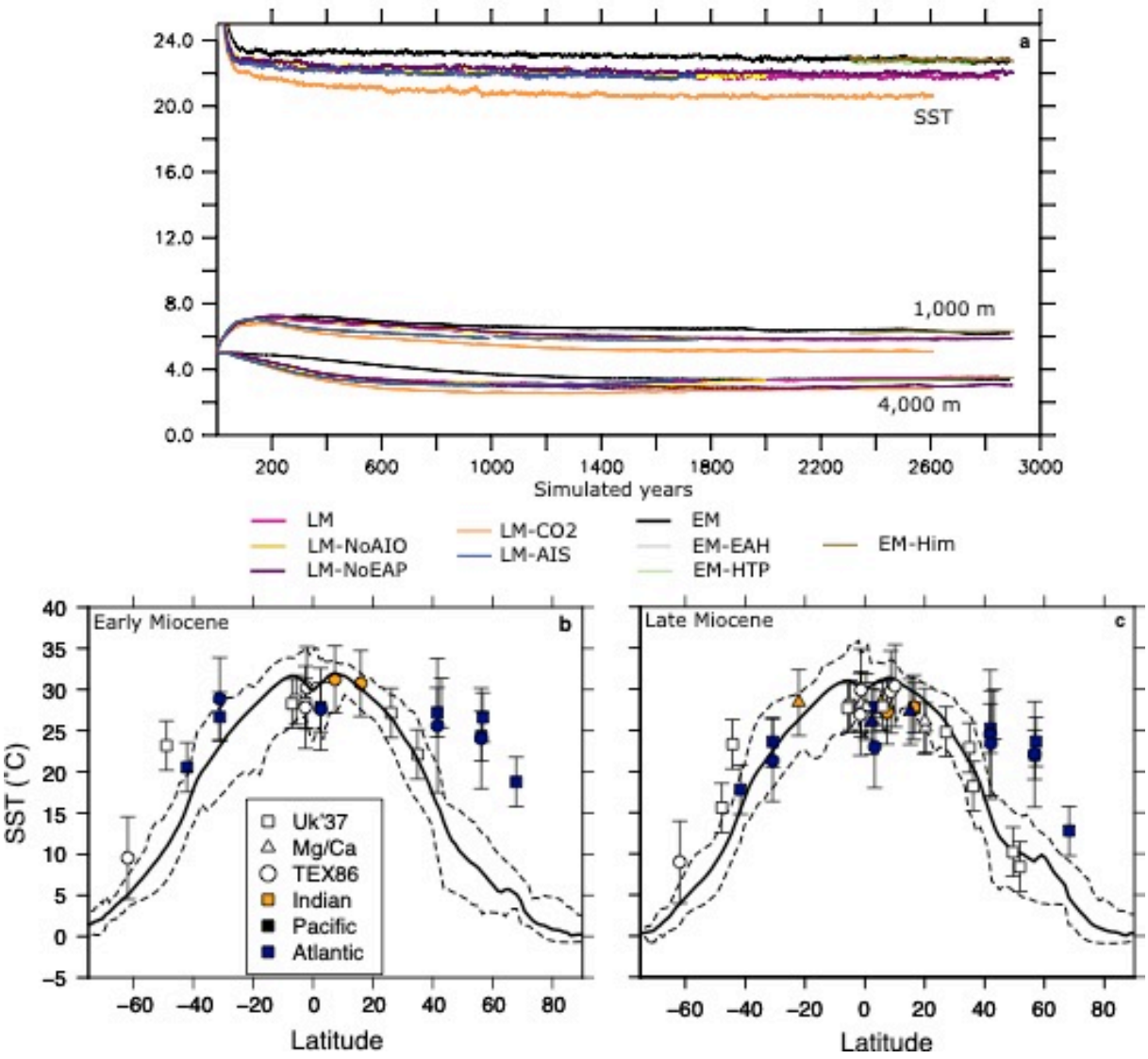

Extended Data Figure 9: Simulation equilibrium and zonal mean temperature gradient. a) Global ocean temperature evolution at the sea surface, in intermediate (1,000 m) and deep waters (4,000 m) for late Miocene (LM) and early Miocene (EM) simulations, and sensitivity experiments. Zonal mean SST gradient for EM (b) and LM (c) simulations compared to available proxy estimation. Bold line indicates mean annual SST, dashed line depicts minimum and maximum value for each latitude. Temperature reconstruction are from ref. 45 , based on compilation by ref. 83 and additional information on the compilation can be found in ref. 45.